

2003

## Net Surface Flux Budget Over Tropical Oceans Estimated from the Tropical Rainfall Measuring Mission (TRMM)

Tai-Fang Fan

*College of William & Mary - Arts & Sciences*

Follow this and additional works at: <https://scholarworks.wm.edu/etd>



Part of the [Atmospheric Sciences Commons](#)

---

### Recommended Citation

Fan, Tai-Fang, "Net Surface Flux Budget Over Tropical Oceans Estimated from the Tropical Rainfall Measuring Mission (TRMM)" (2003). *Dissertations, Theses, and Masters Projects*. Paper 1539626825.  
<https://dx.doi.org/doi:10.21220/s2-jkeh-w028>

This Thesis is brought to you for free and open access by the Theses, Dissertations, & Master Projects at W&M ScholarWorks. It has been accepted for inclusion in Dissertations, Theses, and Masters Projects by an authorized administrator of W&M ScholarWorks. For more information, please contact [scholarworks@wm.edu](mailto:scholarworks@wm.edu).

**NET SURFACE FLUX BUDGET OVER TROPICAL OCEANS  
ESTIMATED FROM THE TROPICAL RAINFALL MEASURING  
MISSION (TRMM)**

---

A Thesis

Presented to

The Faculty of the Department of Applied Science

The College of William and Mary in Virginia

In Partial Fulfillment

of the Requirements for the Degree of

Master of Science

---

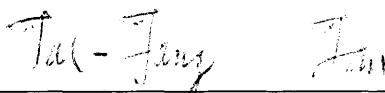
by

Tai-Fang (Alice) Fan

2003

## APPROVAL SHEET

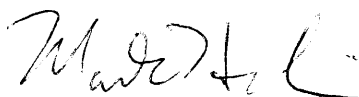
This thesis is submitted in partial fulfillment of  
the requirements for the degree of  
Master of Sciences



---

Tai-Fang (Alice) Fan

Approved, June 2003



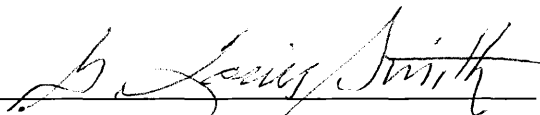
---

Dr. Mark Hinders  
Associate Professor of Applied Science  
The College of William & Mary in Virginia



---

Dr. Bing Lin  
Research Physical Scientist  
Radiation & Aerosols Branch, NASA Langley Research Center



---

Dr. Louis Smith  
Research Professor  
Virginia Polytechnic Institute and State University



---

Dr. Paul W. Stackhouse, Jr  
Senior Research Scientist  
Radiation & Aerosols Branch, NASA Langley Research Center

## TABLE OF CONTENTS

	Page
Acknowledgements	v
List of Tables	vi
List of Figures	vii
Abstract	x
Chapter 1. Introduction	2
Chapter 2. Instruments and Data Sets	9
2.1 VIRS	9
2.2 CERES	10
2.3 TMI	11
2.4 Rainfall Data Set	12
2.5 Ancillary Data Set	13
Chapter 3. Flux Retrieval Algorithm	14
3.1 Radiation Fluxes	14
3.2 Turbulent Fluxes - Latent and Sensible Heat	15
3.3 Rain-induced Sensible Heat Flux	18
3.4 Sensitivity test	21

Chapter 4. Validation and Comparison of Turbulent Fluxes	25
4.1 Ship Validation	25
4.2 Satellite Comparison	29
Chapter 5. Net Surface Fluxes	36
5.1 Shortwave Radiation	36
5.2 Longwave Radiation	36
5.3 Wind Speed	39
5.4 Humidity	40
5.5 Latent Heat Fluxes	43
5.6 Sensible Heat Fluxes	45
5.7 Net Surface Fluxes	47
Chapter 6. Summary and Conclusion	51
List of References	53
Appendix A. Facts about TRMM Mission and Its Instruments	58
Vita	63

## ACKNOWLEDGEMENTS

I wish to express my sincere gratitude to Dr. Lin for his guidance throughout this research project. Our numerous and often lengthy discussions and his patient reviews and criticism of the manuscript were invaluable. I also wish to thank my other thesis committee members Drs. Mark Hinders, Louis Smith, and Paul Stackhouse for their in-depth reviewing of the manuscript and helpful suggestions.

I would like to thank the Goddard DAAC for the ease of data ordering. I also like to thank my co-workers Thomas Caldwell for providing ancillary data in a timely fashion, and Joe Stassi for proof reading.

## LIST OF TABLES

Table	Page
1. Spectral characteristics and nadir field-of-view for VIRS, CERES, and TMI	12
2. Latent heat statistics from satellite COARE estimation and ship (COV, ID, bulk) measurements.	27
3. Sensible heat statistics from satellite COARE estimation and ship (COV, ID, bulk) measurements.	27
4. Seasonal mean for shortwave, longwave, latent, sensible, and net surface heat fluxes	50

## LIST OF FIGURES

Figure	Page
1. Instantaneous rain-induced sensible heat for August 1998 from TRMM	20
2. Gridded averages of rain-induced sensible heat for August 1998 from TRMM	21
3. Sensitivity tests of sensible and latent heat fluxes by varying wind speed, surface temperature, and air temperature (k)	23
4. Distribution of latent heat versus wind speed for June - August 1998	24
5. Distribution of latent heat versus surface and air specific humidity difference for June - August 1998	24
6. Distribution of latent heat versus air specific humidity distribution for June - August 1998	24
7. Satellite estimates versus ship (NAURU99) measurements	28
8. Zonal averages of latent heat flux for TMI and SSM/I	32
9. Gridded averages of latent heat flux for TMI and SSM/I	33
10. Zonal averages of sensible heat flux for TMI and SSM/I	34
11. Gridded averages of sensible heat flux for TMI and SSM/I	35
12. Estimation of net surface shortwave fluxes from TRMM	37
13. Occurrence and diurnal variation of net surface shortwave fluxes from TRMM for June-August 1998	37
14. Estimation of net surface longwave fluxes from TRMM	38



15. Occurrence and diurnal variation of net surface longwave fluxes from TRMM for June-August 1998	39
16. Diurnal variation of net longwave surface fluxes from TRMM for June-August 1998	39
17. Wind speed distribution from TRMM satellite	40
18. Surface specific humidity distribution from TRMM	41
19. Air specific humidity distribution from TRMM	41
20. Surface and air specific humidity difference ( $Q_s - Q_a$ ) from TRMM	42
21. Diurnal variation of wind speed and humidity from TRMM for June-August 1998	42
22. Estimation of latent heat fluxes from TRMM	43
23. Occurrence and diurnal variation of latent heat fluxes from TRMM for June-August 1998	44
24. Diurnal variation of latent heat fluxes, wind speed, and $Q_s - Q_a$ from TRMM for June-August 1998	44
25. Estimation of sea surface temperature from TRMM	45
26. Surface and air temperature difference from ECMWF	46
27. Estimation of sensible heat fluxes from TRMM	46
28. Diurnal variation of sensible heat fluxes and wind speed from TRMM, and $T_s - T_a$ from ECMWF for June-August 1998	47
29. Estimation of net surface fluxes from TRMM	49

30. Occurrence and diurnal distribution of net surface heat fluxes from TRMM for June-August 1998	49
31. Zonal mean estimation of surface net fluxes from TRMM	50

## ABSTRACT

Energy exchanges between the atmosphere and oceans involve several complicated processes: shortwave (SW) and longwave (LW) radiative processes, sea surface turbulent latent heat and sensible heat transports, and rain induced sensible heat fluxes. This study investigates these flux components over tropical oceans (30°N to 30°S) using data collected from the Tropical Rainfall Measuring Mission (TRMM) which is equipped with five sensors: Visible and Infrared Scanner (VIRS), Clouds and Earth's Radiant Energy System (CERES), TRMM Microwave Imager (TMI), Precipitation Radar (PR), and Lightning Imaging Sensor (LIS). The data from VIRS, CERES, and TMI instruments are used in this study. The LW and SW net fluxes are estimated by the CERES project with an accuracy of  $\sim 2$  and  $\sim 3 \text{ W/m}^2$  at the top of atmosphere and  $\sim 8$  and  $\sim 15 \text{ W/m}^2$  at sea surfaces, respectively.

The turbulent latent and sensible heat fluxes from oceans to the atmosphere are calculated from TMI retrievals of near sea surface wind speeds, air humidity, and temperature formulae derived from Tropical Ocean Global Atmosphere (TOGA) Coupled Ocean-Atmosphere Response Experiment (COARE). The latent and sensible heat fluxes have been compared to those of the Goddard Satellite-based Surface Turbulent Fluxes version 2 (GSSTF-2) product derived from Special Sensor Microwave/Image (SSM/I) data collected by Defense Meteorological Satellite Program (DMSP) satellites. The results show that the monthly averaged differences for the whole tropical oceans range from  $-7$  to  $2 \text{ W/m}^2$  and  $-6$  to  $-8 \text{ W/m}^2$  for latent heat and sensible heat for the first eight months of 1998. The sensible heat from TMI are lower than those from GSSTF-2 across all compared latitudes which may be due to a positive bias of  $7 \text{ W/m}^2$  in the GSSTF-2. The TRMM satellite derived turbulent fluxes are about  $1.9 \text{ W/m}^2$  and  $1.64 \text{ W/m}^2$  lower for latent heat and sensible heat fluxes when comparing with in-situ ship measurements. Rain droplets are the condensation of vapor into water or ice at the upper troposphere. They are usually cooler than sea surface temperature, therefore have cooling effects on the surface. The rain induced sensible heat fluxes are estimated from the TMI rainfall Profiling data.

Combining all these fluxes, the zonal averaged Net Surface Fluxes (NSF) from oceans to the atmosphere varies from  $-100$  to  $100 \text{ W/m}^2$  over tropical oceans. From the equator toward 30° the NSF stays at approximate  $100 \text{ W/m}^2$  in the summer hemisphere and gradually drops from  $100$  to  $-100 \text{ W/m}^2$  in the winter hemisphere. The positive tropical total NSF is generally balanced by ocean heat storage in term of mixing layer temperature change, the loss of fluxes in higher latitudes, and oceanic vertical heat transports.

**Net Surface Flux Budget Over Tropical Oceans Estimated  
from the Tropical Rainfall Measuring Mission (TRMM)**

## INTRODUCTION

The Tropical Rainfall Measuring Mission (TRMM) is the first satellite to carry all the instruments needed to estimate the major radiation and turbulent fluxes at sea surface, top-of-atmosphere (TOA), and within atmosphere simultaneously. The net surface shortwave flux is the heat source for ocean surface, and the rest (net longwave, latent heat, and sensible heat fluxes) are generally heat losses from sea surface to the atmosphere in the Tropics. These fluxes are critical parameters for coupled ocean-atmosphere circulation models. Due to the processing orbit, TRMM provides a unique opportunity to examine the diurnal variations of radiation budget, latent and sensible heat fluxes, and air-sea interactions.

Shortwave (SW) radiation from the Sun is the heat source for the Earth. In response, the Earth emits thermal radiation, mostly in the infrared part of the spectrum back to space. The balance between incoming and outgoing energy is the Earth's Radiation Budget (ERB). Thick low clouds reflect more SW radiation back to space than the dark surface, and emit longwave (LW) radiation like a surface. Thus, they have cooling effects on the climate. On the other hand, high thin clouds allow most solar radiation to pass through and trap significant amounts of the emitted LW flux, therefore they have warming effects on the Earth. Since cloud optical and physical properties, such as cloud height, thickness, temperature, fractional coverage, phase, effective particle size, and optical depth greatly affect the ERB, to accurately calculate the surface flux requires a detailed knowledge of how clouds absorb and reflect incoming SW solar energy, as well as how they absorb and reemit outgoing LW energy. In order to obtain radiative fluxes under both clear and cloud conditions, the International Satellite Cloud Climatology Project (ISCCP) uses a two channel threshold cloud detection technique (Rossow, 1990, 1995; Zhang, 1995) plus cloud optical depth and particle size to calculate radiative fluxes based on data collected from geostationary and polar orbital satellites. The Cloud and Earth's Radiant Energy System (CERES) project uses all five narrowband channels of

Visible and Infrared Scanner (VIRS) to derive the cloud properties. The details about the techniques are described in later sections and in the papers of Minnis (1995, 1997, 1998, 2001, 2002). The three broadband channels of CERES instrument are designed to provide the most accurate estimates of solar and thermal infrared radiative fluxes (SW and LW) at the surface, TOA, and several levels within the atmosphere (Wielicki, et al., 1996) by considering cloud and atmosphere effects. Simultaneous measurements of cloud properties and broadband radiative fluxes provide the basis for accurate modeling of both cloud and radiation processes in climate models.

Besides radiative energy exchanges between the sea and atmosphere interface, there are turbulent heat fluxes, and rain-induced sensible heat transports. Because of the temperature, humidity, and wind stress difference between the sea skin and the atmosphere above the sea surface, turbulent processes are produced within the air-sea interface. The turbulence continually mixes warm humid air parcels at the sea skin with cool dryer air parcels from the upper atmosphere layers. As a result, both moisture and sensible heat fluxes are transported from the sea surface into the atmosphere. This dynamics caused by the humidity and temperature difference between the air and sea surface is enhanced by near sea surface wind speed and the wind induced sea surface roughness. Since the moisture within the humid air parcel is originally evaporated from the sea surface water, the moisture (or water vapor) flux is also called latent heat flux, an energy measure of the thermodynamic phase change from water to vapor. Direct turbulent fluxes can be observed by measuring the time and space series of turbulent velocity in vertical direction and the variables of interest. Since it is difficult, expensive, and impractical to measure the required variables over large horizontal, vertical, and temporal scales, the bulk formulae based on applications of the Monin-Obukhov similarity theory (MOST) are the alternate approach. MOST is based on the statistical average of small-scale heat transports by turbulence. The bulk algorithm used in this study is developed by Fairall et al. (1996) and based on the Tropical Ocean Global Atmosphere (TOGA) Coupled Ocean-Atmosphere Response Experiment (COARE). In the Tropics, the latent heat flux is comparable to net surface SW flux, and the sensible

heat budget is about one order of magnitude smaller than the latent heat budget.

Three-fourth of the weather-producing atmospheric heating energy comes from the release of the latent heat of condensation in the process of precipitation (Kummerow, 1998). The energy released by precipitation affects the entire global circulation. An estimated two-thirds of the global precipitation falls in the Tropics. The variability of tropical rainfall affects the lives and economics of more than half of the world's population. The cumulus heating is one of the principal driver of regional and global-scale atmospheric circulations. However, the large spatial and temporal variability of rainfall systems poses a major challenge to estimate total global rainfall. Previous rainfall measurements are incomplete in their global coverage and inadequate to describe the large variations that occur in the Tropics. Before TRMM, there was a great degree of uncertainty in rainfall estimates. The quantitative estimates of tropical precipitation vary by as much as 100% (Kummerow, 1998). These measurements cannot capture the significant structural variations that occur in heating and cooling profiles between convective and stratiform rainfall regions. The primary goals of TRMM are the intensive and global measurements of tropical rainfall rates and the use of an active microwave instrument, Precipitation Radar, to calibrate passive instruments in precipitation estimations. TRMM, a flying rain gauge, provides calibration or adjustment to the rain estimates inferred from other satellite measurements. Since the TRMM launch, the relative errors of precipitation rates in gridded monthly means are significantly reduced to about 20%. Rain is episodic and violent in the Tropics. The largest hourly rain rate observed by the ship R/V Moana Wave during the TOGA COARE intensive observation period (IOP) is  $1.5 \times 10^{-2} \text{ kg /m}^2\text{s}$  (Gosnell, 1995), which induces a sensible heat of  $\sim 250 \text{ W/m}^2$ , a non-negligible value. But its amount is about two orders smaller than the latent heat flux after averaging into monthly and gridded means.

There have been many attempts by scientists to determine the surface flux of radiation, moisture, sensible heat, and momentum at the air-sea interface. For example, Gautier et al. (1988) attempted to calculate the surface total heat budget over Indian ocean during the 1979 monsoon. Liu et al. (1988, 1990) retrieved latent heat fluxes for tropical

Pacific ocean from 1980 to 1983. Michael and Nunez (1991) estimated monthly mean values of radiative and turbulent heat fluxes at the ocean surface near John Brewer Reef, Australia from June 1, 1985 to April 11, 1986. Rain induced sensible heat in tropical oceans was investigated by Gosnell et al. (1995). Clayson and Curry (1996) determined the surface turbulent fluxes and Schule et al. (1997) evaluated daily mean latent heat over TOGA COARE region, respectively. Chou et al. (1998) calculated the radiation budget over the Pacific warm pool for the TOGA COARE. Curry et al. (1999) determined all the flux components for TOGA COARE. Mahrt (2001) calculated area-averaged turbulent fluxes using data from Boreal Ecosystem-Atmosphere Study. All the above attempts were either limited to small regions or to certain components of the heat fluxes. Many of these studies needed to assemble data from different sources, so that the temporal and spatial mismatches could impair the accuracy.

Global scale radiation budget has been estimated by ISCCP, Earth Radiation Budget Experiment (ERBE), Surface Radiation Budget (SRB) project in association with the World Climate Research Programme/Global Energy and Water Cycle Experiment (WCRP/GEWEX), and CERES projects. ISCCP has computed the surface radiation fluxes every 3 hours in  $2.5^\circ$  by  $2.5^\circ$  grid boxes from 1983 to 2001 (Rossow and Zhang, 1995) using data collected from geostationary satellites (METEOSAT, GOES, GMS, INSAT) and NOAA polar orbiters (NOAA-8 to NOAA-14). ERBE provided global top-of-atmosphere (TOA) radiation fluxes and albedos using data from the Earth Radiation Budget Satellite (ERBS), NOAA-9, and NOAA-10 from 1984 through 1999. The SRB project at NASA Langley produces surface and TOA radiation budget in  $1^\circ$  by  $1^\circ$  grids from 1984 through 1993 (Stackhouse et al. 2000) using ISCCP and ERBE data. CERES measures the radiation at TOA, and calculates LW and SW heating and cooling rates at several levels within the atmosphere and at the Earth's surface using data from TRMM, Terra, and Aqua satellites since 1998.

Currently, there are several global turbulent flux data sets available. Five of them are derived from satellite measurements and two of them are from atmospheric model reanalyses. The five satellite estimates include the Hamburg Ocean Atmosphere



Parameters from Satellite (HOAPS), Japanese Ocean Flux data set with Remote sensing Observations (J-OFURO), Goddard Satellite-based Surface Turbulent Fluxes (GSSTF-2), Artificial Neural Network (ANN) estimated turbulent fluxes, and TRMM Microwave Imager (TMI) estimated Turbulent Fluxes in this study (hereinafter called TMITF). They all use Special Sensor Microwave/Imager (SSM/I) measurements and daily or weekly mean of surface temperature except TMITF which uses TMI measurements and its retrieval of temperature and wind speed. The two model reanalyses are the National Center for Environmental Prediction (NCEP) reanalysis and the European Centre for Medium-Range Weather Forecasts (ECMWF) reanalysis.

The HOAPS uses data collected from SSM/I and AVHRR to estimate moisture fluxes. The sea surface temperature used was daily mean products from NOAA/NASA Ocean Pathfinder. This data set covers global oceans with three different spatial resolutions ( $0.5^\circ$ ,  $1.0^\circ$ , and  $2.5^\circ$ ) and three different time resolutions (day, pentad, and month) from 1987 to 1997. The J-OFURO data set (Kubota et al., 2002) calculates turbulent heat fluxes from 1991 to 1995 for the whole globe using data from SSM/I. Their temporal and spatial resolutions are monthly and  $1^\circ$  by  $1^\circ$  grids, respectively. J-OFURO uses the climatologic monthly means of pressure and air density, weekly gridded means of sea surface temperature provided by NCEP, wind speed from Wentz (1997), and the Qa algorithm from Schluessel et al. (1995) to calculate latent and sensible heat fluxes. The GSSTF-2 data set also uses Wentz algorithm for wind speed, but the temperatures at sea surface and 2-meter height and surface pressure are daily mean values from NCEP, and the Qa algorithm is from Schulz et al. (1993). This product consists of  $1^\circ$  by  $1^\circ$  gridded daily means and covers global oceans from July 1987 to December 2000 (Chou et al., 1998; 2003). The ANN turbulent heat flux product from the Institute for Computational Earth System Science (ICESS) at University of California Santa Barbara (Jones et al., 1999) is derived from a combination of sea surface temperature from NCEP reanalysis, total precipitable water and surface wind speeds from SSM/I, and surface specific humidity and air temperature from an artificial intelligence approach. This product is currently available over the tropical Pacific basin ( $110^\circ$  E- $290^\circ$  E;  $30^\circ$  S-  $30^\circ$  N)

for the years 1998 through 2000. The main characteristics are daily, pentads, and monthly temporal resolutions in  $0.25^\circ$  by  $0.25^\circ$  spatial grids.

Significant differences are found among these global scale data sets (Kubota et al., 2002; Chou et al., 2003) and between reanalysis and in-situ measurements (Josey, 2001; Moore et al., 2002). The NCEP and ECMWF reanalysis data sets overestimate latent heat flux when compared to ship measurements at Northeast Atlantic (Kubota et al., 2002; Josey 2001). NCEP under-estimates the surface air temperature (Smith et al., 2001; Wang and McPhaden, 2001; Chou 2003), which causes GSSTF-2 to over-estimate sensible heat by  $7\text{W/m}^2$ . Studying the HOAPS data set, Schluessel et al. (1995) and Schulz et al. (1997) found that the HOAPS estimates usually have  $\sim 30\text{W/m}^2$  uncertainty when compared with instantaneous in-situ measurements. Chou et al. (2003) also suggested that HOAPS under-estimates latent heat flux by  $20\text{-}50\text{W/m}^2$  in the Tropics. The cause is due to an under-estimation of wind speed and the specific humidity difference between sea skin and 10-m air. The sea surface turbulent flux (SEAFLEX) project has been established to conduct inter-comparison studies among different flux algorithms, available turbulent flux data sets, and input parameters (Curry et al., 2003).

Daily mean is the smallest temporal resolution for the above global data sets. The unique feature of the TMITF is its use of concurrent wind speed, humidity, and temperature to calculate turbulent fluxes and to allow the study of diurnal variations and local events. The advantages of simultaneously retrieving the major components of sea surface fluxes using TRMM data include better spatial and temporal collocation and thus more accurate net surface flux estimates. TMITF covers tropical oceans ( $180^\circ\text{E}$ - $180^\circ\text{W}$ ,  $30^\circ\text{S}$ - $30^\circ\text{N}$ ) from January to August 1998 and from June to August 1999, and it will be extended to cover from January 1998 to December 2001 in the near future. The basic temporal and spatial resolutions are hourly and  $1^\circ$  by  $1^\circ$  grids, respectively. They can be averaged into daily, monthly, and seasonal averages by users. Along with TMITF turbulent fluxes, SW and LW fluxes at TOA and surface were calculated from CERES and VIRS measurements from January to August 1998. Currently only TRMM provides the opportunity to calculate both radiation and moisture fluxes over oceans using

instruments onboard the same satellite. Although TRMM is designed primarily for precipitation research, this study uses its measurements to retrieve net surface fluxes and provides hourly, daily, and monthly gridded and zonal means for the major components of the surface heat fluxes over tropical oceans. Chapter 2 describes the instruments and data sets used. Chapter 3 explains the retrieval algorithms and sensitivity test. Chapter 4 compares the results with ship measurements and satellite derived GSSTF-2 data set. Chapter 5 discusses the results of net surface flux budget including all the major heat components. Their geographical distributions and diurnal variations are addressed. Finally, the conclusions are given in chapter 6. For reference, some basic information about TRMM and its instruments are given in appendix A.

## CHAPTER 2

### INSTRUMENTS and DATA SETS

TRMM is a joint project between the US National Aeronautics and Space Administration (NASA) and the National Space Development Agency of Japan to measure the tropical rainfall distribution (Kummerow et al. 1998). The TRMM satellite was launched from Tanegashima Island on November 27, 1997, and has been flying in a precessing orbit with a  $35^\circ$  inclination at approximately 350km altitude. The precessing orbit allows the satellite to observe the entire diurnal cycle in 46 days at each position over the Tropics, which provides a unique opportunity to examine the diurnal variations of radiative fields and air-sea interactions. The TRMM satellite is equipped with five sensors: Visible and Infrared Scanner (VIRS), Clouds and Earth's Radiant Energy System (CERES), TRMM Microwave Imager (TMI), Precipitation Radar (PR), and Lighting Imaging Sensor (LIS). TMI and VIRS instruments have been working well since TRMM launched in November 1997. The CERES instrument on TRMM was turned off after August 1998 and was turned back on in March 2000 to overlap with the CERES instruments onboard the Terra satellite. This study uses the data collected from the VIRS, CERES, and TMI instruments to estimate radiation (SW and LW) and turbulent (latent and sensible) fluxes for the first eight months of 1998. The spectral characteristics for these three instruments are listed in Table 1.

#### 2.1 VIRS

VIRS is a five-channel (0.63, 1.6, 3.75, 10.8, and  $12.0\mu\text{m}$ ) narrowband imaging spectral radiometer with a 2km nadir field-of-view (FOV) and a swath width of  $\sim 720\text{km}$ . It senses radiation coming up from the Earth at the five wavelengths. The shortwave channels at 0.63, 1.61, and  $3.75\mu\text{m}$  wavelength measure Earth-reflected solar with some Earth-emitted radiation. The two infrared channels at 10.8 and  $12.0\mu\text{m}$  wavelength measure Earth-emitted thermal radiation. With the correction for atmosphere gas

absorption, the temperature measurements correspond primarily to the emission of the earth surface for clear skies, and tend to be the cloud top temperatures under cloudy conditions.

Since cloud properties have a significant effect on radiative fluxes, the CERES project uses the VIRS data to derive cloud mask (clear or cloudy), cloud temperature, height, thickness, pressure, layering, optical depth, emissivity, particle phase (water or ice) and effective size, and liquid/ice water path (Minnis et al., 1995, 1997, 1998). Different techniques are applied to day and night time measurements separately. The visible infrared solar-infrared split-window technique (VISST) is used during day time, and the solar-infrared infrared split-window technique (SIST) is used during night time (Minnis et al., 2002). Ancillary data, skin temperature and temperature and humidity profiles, from ECMWF reanalyses are used in the derivation process. These cloud parameters are collocated and convolved over the CERES FOV (10-20 km) using CERES point spread function (Smith, 1994).

## **2.2 CERES**

The CERES instrument is a three-channel broadband radiometer with SW channel of 0.3-5  $\mu\text{m}$ , window channel of 8-12 $\mu\text{m}$ , and total channel of 0.3-200 $\mu\text{m}$  (Lee et al.1996). It measures the radiation from ultraviolet through far-infrared spectral regions and provides estimates of global radiation energy budget at TOA. The SW detector measures Earth-reflected solar and Earth-emitted infrared radiation, while the total channel detects both solar and terrestrial radiation. The LW measurements are obtained from the differences between the total and SW channels. The first CERES instrument was launched onboard the TRMM spacecraft in November 1997. After that, four more CERES instruments were launched into polar orbits: two on board the Earth Observing System (EOS) Terra satellite launched on December 18, 1999, and the other two on board EOS Aqua satellite launched on May 4, 2002. The CERES instrument has a 10km nadir FOV for TRMM, and 20 km FOV for Terra and Aqua. Follow-up CERES satellite missions are planned to create a continuous 15-year history of highly accurate radiation

energy budget and cloud data for enhanced climate analyses.

Using information from the VIRS measurements on the TRMM spacecraft and the Moderate-Resolution Imaging Spectroradiometer (MODIS) instruments on the Terra and Aqua spacecraft, the CERES project determines various cloud properties. MODIS, with 36 spectral channels, is an expanded version for VIRS. These properties and external ancillary temperature and moisture profiles from ECMWF are critical for calculating the surface radiation fluxes. Besides direct measurements of reflected SW, emitted LW, and thermal window radiances, estimates of SW and LW fluxes at TOA and surface, and observational geometries, the Single Scanner Footprint (SSF) data products of the CERES project also contain temporally and spatially coincident VIRS or MODIS imager-based radiances and their derived cloud properties. The flux parameters at the surface include upward, downward, and net SW and LW radiative fluxes. Each SSF file contains information for a single hour and a single CERES instrument mounted on one satellite. The combined multiple instrument/satellite data are available in the monthly average products: Synoptic Radiative fluxes and Clouds (SYN), and Regional, Zonal, and Global Averages (AVG/ZAVG). CERES data products range from a single CERES FOV at ~10km to 1 degree gridded data over the globe. Time scales range from instantaneous radiative fluxes, 3 hourly averages, to daily and monthly averages. For more information, visit the CERES web site at <http://asd-www.larc.nasa.gov/ceres>.

## **2.3 TMI**

Surface temperature, air humidity, and wind speed are required parameters for use of the bulk formula to estimate turbulent latent and sensible heat fluxes. Although infrared measurements can be used to estimate surface temperature for clear skies, they cannot provide these values under cloudy conditions. Further more, wind speed and air humidity are usually estimated through microwave sensors. Three kinds of microwave sensors (scatterometer, altimeter, and radiometer) are frequently used to measure wind speeds

over oceans. TMI is a nine-channel passive microwave radiometer with vertically and horizontally polarized channels at frequencies 10.65, 19.35, 37, and 85.5GHz, and one vertically polarized channel at 21.3GHz. The spatial resolutions range from 7.2km by 4.4km to 63.2km by 38.2km, depending on wavelengths (see table 1). The conical scan at  $\sim 53^\circ$  incident angle of TMI results a swath width of approximately 760 km. Brightness temperature (BT) measurements are provided at 104 scan positions for the low frequency channels and at 208 scan positions for the highest frequency (85.5GHz) channels. The BT values measured by these nine channels are used to retrieve sea surface temperature (Ts), near-surface air humidity (Qa), and wind speed (WS) in this study. These parameters are then used to calculate the turbulent latent heat and sensible heat fluxes. The TMI data are stored and distributed at the Goddard Distributed Active Archive Center (DAAC). The data used in this study are level 1, orbital BT measurements.

Table 1. Spectral characteristics and size of nadir field-of-view for VIRS, CERES, and TMI

VIRS	Wave length	0.63 $\mu\text{m}$	1.6 $\mu\text{m}$	3.75 $\mu\text{m}$	10.8 $\mu\text{m}$	12.0 $\mu\text{m}$
	Nadir FOV	2 km	2 km	2 km	2 km	2 km
CERES	Wave length	0.3–5 $\mu\text{m}$	8–12 $\mu\text{m}$	0.3–50 $\mu\text{m}$		
	Nadir FOV	10 km	10 km	10 km		
TMI	Wave length	10.65 GHz	19.35 GHz	21.30 GHz	37.00 GHz	85.5 GHz
	Nadir FOV	63.2 km $\times$ 38.2 km	30.4 km $\times$ 18.4 km	27.2 km $\times$ 16.5 km	16.0 km $\times$ 9.7 km	7.2 km $\times$ 4.4 km

## 2.4 Rainfall Data Set

Latent heat released by the phase changes from water vapor to liquid water or ice is the most important contribution to the heating of atmosphere. Rainfall is related to the latent heat transported from the surface to the atmosphere. Rainfall amounts directly measure the heating of the atmosphere. This heating is an energy source of the global

atmospheric circulation. Scarcity of quantitative precipitation information has been a bottleneck for atmospheric science. The primary rainfall instruments on TRMM are TMI, PR, and VIRS. The combination of satellite passive (TMI and VIRS) and active (PR) sensors provides critical information regarding the three-dimensional distributions of precipitation and heating in the Tropics. The frequency dependence of electromagnetic properties of cloud and precipitation particles allows the passive microwave radiometers to sound the different depths in a precipitation cloud, but the height assignment of cloud properties is not very specific. On the other hand, active microwave sensors provide specific height information based upon the time delay of the backscattered radar radiation. VIRS retrieves cloud-top temperatures and structures to complement the other two sensors. By using these three instruments, TRMM obtains the first detailed and comprehensive rainfall data sets. The data used in this study are the level 2 TMI Profiling data. They have vertical hydrometer profiles and surface rain rates on a pixel by pixel basis. These precipitation data are used in estimations of rain-induced sensible heat fluxes. This data product was also ordered from Goddard DAAC.

## **2.5 Ancillary Data Set**

Since satellites cannot provide all the parameters needed to calculate the heat fluxes, gridded analysis and reanalysis data produced by the ECMWF are used as the ancillary data. ECMWF is an international organization supported by 24 European countries. Their goal is to deliver medium-range weather forecasts. Among many estimated meteorological parameters, the temperature and humidity profiles of ECMWF are used for the retrievals of cloud properties and for the calculating of surface SW and LW radiation. The skin and air temperature differences are used to obtain near surface air temperature in the estimations of turbulent sensible heat fluxes.



## CHAPTER 3

### FLUX RETRIEVAL ALGORITHM

The net surface flux (NSF) into the ocean is given as:

$$\text{NSF} = H_{\text{SW}} + H_{\text{LW}} - H_{\text{LAT}} - H_{\text{SEN}} - H_{\text{RAIN}} \quad (1)$$

where  $H_{\text{SW}}$ ,  $H_{\text{LW}}$ ,  $H_{\text{LAT}}$ ,  $H_{\text{SEN}}$ , and  $H_{\text{RAIN}}$  are net SW, net LW, turbulent latent heat, turbulent sensible heat, and rain-induced sensible heat fluxes, respectively. Note that net  $H_{\text{SW}}$  and net  $H_{\text{LW}}$  are defined as (downward – upward) radiation in the CERES project. A positive value means a heat gain for oceans. Therefore, net  $H_{\text{LW}}$  usually has negative values. Net  $H_{\text{LW}}$ ,  $H_{\text{LAT}}$ ,  $H_{\text{SEN}}$ , and  $H_{\text{RAIN}}$  are generally a heat loss for sea surface. An overall positive NSF indicates that the ocean gains heat fluxes, and a negative value implies that the ocean loses heat fluxes. The calculations of each component are explained in the following sections.

### 3.1 Radiation Fluxes

The CERES project is designed to monitor the TOA radiation budget, define the physical properties of clouds, estimate the surface radiation budget, and determine the divergence of energy within the atmosphere. CERES retrieves TOA radiative fluxes from the measured radiances using Angular Distribution Models (ADM) for SW, LW, and window channels (Loeb et al. 2001, 2003). The surface radiative fluxes are estimated based on several models. The first surface SW algorithm was based on an empirical relationship between the TOA fluxes and the measured surface radiation budget components from the Baseline Surface Radiation Network (BSRN) and the Atmospheric Radiation Measurement (ARM) programs. The first surface LW algorithms started with the window channel where longwave is unimpeded. These algorithms have been extended to include factors such as water vapor, solar zenith angle, cloud properties

(cloud optical depth, particle size, and cloud top temperature derived from VIRS), and meteorological data (surface temperature and humidity from ECMWF) because the surface fluxes are affected by both TOA fluxes and atmospheric conditions. To preserve historical continuity, some parts of the CERES data reduction use algorithms identical to those used in ERBE. At the same time, many of the algorithms on CERES are new. The current models for clear-sky only condition (model A) are from Li et al. (1993) for SW, and from Inamdar and Ramanathan (1997) for LW. The models for all-sky condition (model B) are from Darnell et al. (1983) and Gupta et al. (2001) for SW, and from Gupta (1989) and Gupta et al. (1992) for LW. These models are named Langley Parameterized Shortwave/Longwave Algorithms (LPSA/ LPLA). Detailed descriptions of these algorithms can be found in NASA Technical Publication 2001-211272 and the Algorithm Theoretical Basis Documents of the CERES project (<http://asd-www.larc.nasa.gov/ATBD.html>). The results from these models are inter-compared among themselves and with in-situ measurements over more than thirty sites. The detail results can be found under CERES home page (<http://asd-www.larc.nasa.gov/ceres/ASDceres.html>). This study uses the flux results from model B because it is for all-sky condition. The overall bias (rms) are  $-3.7$  ( $20.6$ )  $\text{W/m}^2$  for LW and  $12.3$  ( $64.6$ )  $\text{W/m}^2$  for SW, respectively (Gupta, et al., 2003). The LW and SW net fluxes estimated by the CERES project are expected to provide an accuracy of  $\sim 2$  and  $\sim 3 \text{ W/m}^2$  at the top of atmosphere and  $\sim 8$  and  $\sim 15 \text{ W/m}^2$  at sea surfaces, respectively (Charlock et al. 2000).

### **3.2 Turbulent Fluxes - Latent and Sensible Heat**

Because remote sensing cannot directly measure turbulent fluxes, an indirect approach through wind speed, humidity, and temperature difference between the sea skin and air at 10 m level is necessary. The retrieval accuracy for each of these parameters is critical for archiving accurate turbulent fluxes. Otherwise, the error propagates through the bulk formula and leads to large errors in the derived turbulent heat fluxes. The

turbulent fluxes estimated in this study use the bulk algorithm based on the stability-dependent aerodynamic model of Tropical Ocean Global Atmosphere (TOGA) Coupled Ocean-Atmosphere Response Experiment (COARE) (Fairall et al., 1996), which was developed using simultaneous flux and bulk meteorological variable measurements combined with the drag transport coefficients from laboratory and theoretical studies of air-sea transfer processes. The TOGA COARE was an observation and modeling program. One of its goals aimed specifically at the determination and interpretation of heat, moisture, and momentum fluxes at the air-sea interface over the west Pacific warm pool region (Coppin 1991, Webster 1992). To reach that goal, an observational network covering a region from 4°S to 2°N and 150°E to 160°E with an intensive observation period (IOP) from November 1992 through March 1993 was set up to collect various flux data. During the three cruise legs made, 1622 fifty-minute averages of heat fluxes and bulk meteorological variables (sea surface and air temperatures, wind speed, wind direction, and water vapor mixing ratio of surface and air) in the wind speed ranging from 0.5 to 10m/s were collected. Various physical processes relating near-surface atmospheric and oceanographic bulk variables and their relationships with the surface fluxes were investigated. Based on the observations and theoretical studies, a bulk parameterization of turbulent fluxes was derived and has been widely validated and used by the SEAFLEX science community. Newly published updates to this COARE bulk algorithm have an accuracy of 5% for wind speeds under 10m/s and 10% for wind speeds between 10 and 20m/s (Fairall, et al., 2003). The later version includes 4439 new values from field experiments by Environmental Technology Laboratory between 1997 and 1999. These new observations have significant cases with wind speed higher than 10m/s. The standard bulk formulae for latent and sensible heat fluxes are:

$$H_{LAT} = \rho L C_L (U_a - U_s)(Q_s - Q_a) \quad (2a)$$

$$H_{SEN} = \rho C_P C_S (U_a - U_s)(T_s - T_a) \quad (2b)$$

where  $\rho$ ,  $L$ ,  $C_L$  and  $C_S$  are air density, latent heat of vaporization, drag transport coefficients of moisture and sensible heat, respectively. Air density is calculated based

on air temperature and a fixed pressure of 1013.25mb. The error caused by fixing the pressure is generally negligible.  $C_p$  is the specific heat of air (1004J/kgK).  $U_a$  is the near-sea surface (10 m above surface) wind speed.  $U_s$  is ocean surface current speed, which is much smaller than  $U_a$  and is assumed to be 0.  $Q_a$  and  $Q_s$  are specific humidity at 10 meters and sea skin, respectively.  $T_a$  and  $T_s$  are potential temperatures at 10 m above and sea skin levels, respectively.  $T_s$  can be estimated by either thermal IR or passive microwave methods, but thermal IR can be obscured by clouds. The advantage of microwave measurements is that they work well for both clear and cloudy skies. The remotely sensed skin temperature is usually colder than the bulk sea surface temperature by 0.2K (Schluessel et al. 1987, 1990). Microwave brightness temperature is relatively insensitive to the atmosphere, but sensitive to surface roughness. Thus it can only be used to retrieve parameters over ocean under no rain condition. The sea surface temperature is estimated empirically by regressing with the BT of non-precipitating measurements in this study. The equation used is:

$$T_s = -223.49 + 2.1094(T_{b10V}) - 0.4187(T_{b10H}) - 1.0339(T_{b19V}) + 0.5966(T_{b21V}) \quad (3)$$

where  $T_{b10V}$  and  $T_{b10H}$  are 10.65GHz vertically and horizontally polarized channels, and  $T_{b19V}$  and  $T_{b21V}$  are 19.35GHz vertical and 21.30GHz vertical channels. Air temperature ( $T_a$ ) is obtained by adding the difference between the sea skin and air (2m) temperatures of ECMWF to the observed sea skin temperature. That is  $T_a = T_s + \text{ECMWF}(T_a - T_s)$ . The air-sea temperature difference is generally very small ( $< 2K$ ) over the open ocean, except for mid-latitudes in the winter hemisphere.

Microwave radiation emitted by the sea surface is strongly dependant on the wind-driven surface roughness offering the possibility to sound the near surface wind speed from a satellite. Using SSM/I data, Goodberlet et al. (1989) and Schluessel and Luthardt (1991) showed that surface wind speed derived from microwave instruments with simple linear retrieval technique has an rms error of 2m/s and 1.4m/s with no bias under weak wind conditions, respectively. This study uses channels of 10.65, 19.35, and 37.0GHz to

calculate the wind speed, and the equation used is:

$$WS = 146.36 + 0.5752(Tb10H) - 0.08165(Tb19H) - 1.3397(Tb37V) + 0.67(Tb37H) \quad (4)$$

The most difficult part for microwave remote sensing is the determination of the sea surface air specific humidity ( $Q_a$ ), which is due to the fact that microwave radiation mainly emerges from entire thick planetary boundary layer. Schulz et al. (1993) found that  $Q_a$  can be estimated with an accuracy of 1.2g/kg from the integrated water vapor content ( $w$ ) of the lowest 500m of the atmosphere using passive microwave (SSM/I) BT measurements. The integrated water vapor value is highly correlated ( $r > 0.9$ ) and linearly related to the specific humidity ( $Q_a$ ) near the sea surface. Later, Schluessel (1996) combined this two-step approach into a one-step optimized approach and corrected the biases in polar ocean basins. It has an accuracy of 1.1g/kg. This study transfers the brightness temperature values between the TMI and SSM/I instruments based on brightness temperature simulations of a microwave radiative transfer model (Lin et al. 1998). Thus, the one-step algorithm is adapted to retrieve surface air specific humidity using TMI observed brightness temperature values. The one-step equation used in this study is:

$$Q_a = -80.23 + 0.6295(Tb19V) - 0.1655(Tb19H) + 0.1495(Tb22V) - 0.1553(Tb37V) - 0.06696(Tb37H) \quad (5)$$

The saturation specific humidity ( $Q_s$ ) at sea surface is essentially a function of the sea surface temperature with a correction factor 0.98 to account for the reduction in the saturated vapor pressure for a 34 parts per thousand salinity (Fairall et al., 1996).

### 3.3 Rain-induced Sensible Heat Flux

Rainfall is the condensation of water vapor into water or ice. The latent heat released from rainfall is very important for tropical climate because two thirds of the world's rainfall in the Tropics. It is one of the primary heat sources driving atmospheric

circulation. Rainfall is related to the amount of fresh water transport from the surface to the atmosphere. In energy cycle, the latent heat fluxes from sea surface evaporation are released through the condensation of vapor to water or ice within the upper troposphere. The majority of these evaporation and condensation processes occur in the Tropics in response to the solar heating. Thus, the Tropics play a key role in the global hydrology and energy cycle.

A raindrop is usually close to thermal equilibrium with its surroundings, with a temperature corresponding to the wet-bulb temperature of the atmosphere at its height. Between cloud base and the near-surface levels, equilibrium occurs for the small droplets, but not the larger droplets. Because rain droplets cannot respond fast enough to the thermodynamic gradients between the near surface air (10m) and the sea skin levels, rain water generally has a different temperature than the sea surface. The rain-induced sensible heat flux is estimated from the rainfall rate and the temperature difference between rain water and surface water. The magnitude of the cooling of the ocean surface and the reduction of the ocean buoyancy depend on both the rain rate and the temperature of the rain droplets when they enter the oceans. Gosnell et al. (1995) and Flament and Sawyer (1995) considered it reasonable to assume that the raindrop temperature is equal to the web-bulb temperature of near sea surface air. Thus, this study assumes that the rain droplets have the wet-bulb temperature of the atmosphere 10 m above the surface as it hits the ocean surface. Since the web-bulb temperature is usually lower than the ocean surface temperature, the rain water generally cools the ocean surface. Because rain rate is a mass flux, the rain-induced sensible heat flux is related to the heat capacity and the temperature difference between rain water and sea surface water. The equation to account for the rain induced sensible heat is:

$$H_{\text{RAIN}} = C_W R (T_s - T_r) \quad (6)$$

where  $C_W$  is the specific heat of water (4186J/kgK),  $R$  is the rain rate in  $\text{kg/m}^2$  per second,  $T_s$  is the bulk sea surface temperature, and  $T_r$  is the rain droplet temperature

when it reaches the surface, which is very close to the wet-bulb temperature at 10m above the surface ( $T_a$ ). A positive  $H_{RAIN}$  is a heat gain for the atmosphere or a heat loss for the ocean. The sensible heat fluxes during intensive convective events have the same order of magnitudes as latent heat fluxes (in hundred Watts per meter square). It is important to determine the degree of cooling associated with rain-induced sensible heat (Gosnell et al., 1995) because of its significance. Figures 1 and 2 show the rain induced sensible heat for August 1998. Figure 1 shows the rain induced sensible heat fluxes for each TMI pixel. Many of the values are more than  $100\text{W/m}^2$ . The negative values are caused by air temperature being higher than surface temperature estimated by ECMWF, which may be caused by hot humid air from warm regions being blown to cooler ocean areas. Figure 2 is a map of the gridded averages of all sky conditions and reveals that there are significant rainfall amounts along the Inter-Tropical Convergence Zone (ITCZ) and South Pacific Convergence Zone (SPCZ), and less rainfall at the subsidence area. Although the rain induced sensible heat is large instantaneously (Fig. 1), it is about two orders of magnitudes smaller than turbulent latent heat and one order of magnitude smaller than turbulent sensible heat (see later sections) when averaged over large spatial and temporal domains.

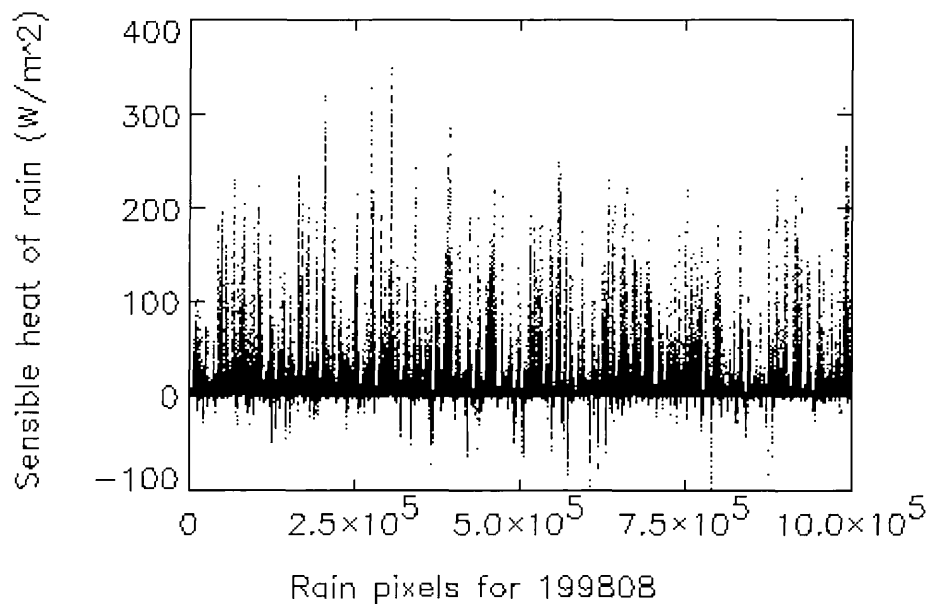


Figure 1. Instantaneous rain-induced sensible heat for August 1998 from TRMM.

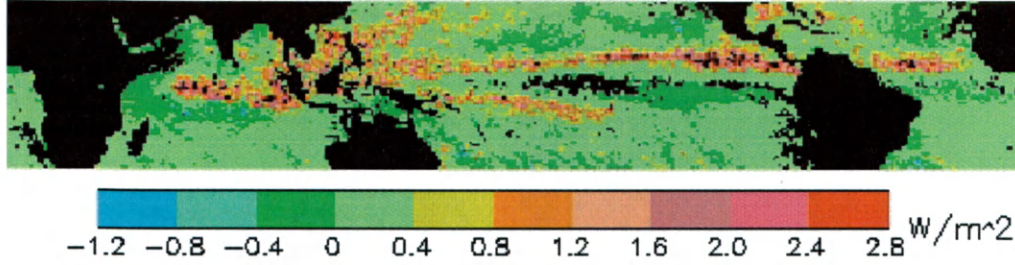


Figure 2. Gridded averages of rain-induced sensible heat for August 1998 from TRMM.

### 3.4 Sensitivity Test

Sensitivity studies test the bias and random errors caused by uncertainties in each of the input parameters. During each sensitivity test, all parameters are kept at the baseline values except the parameter in test. Other sources of errors, such as those from bulk formula are not considered. The accuracy of bulk algorithms can be found in the original studies by Fairall et al. (1996, 2003). There are three parameters each for latent heat and sensible heat flux algorithms (see equations 2a and 2b). Parameters wind speed (WS), sea surface temperature (Ts), and surface air temperature (Ta) are for sensible heat fluxes, and WS, surface specific humidity (Qs), and air specific humidity (Qa) are for latent heat fluxes. Qs is calculated from Ts using the Clausius-Clapeyron equation. The selected baseline values are 6.5m/s, 299K, 298K, and 17g/kg for WS, Ts, Ta, and Qa. The bias (std) of errors associated with these variables are conservatively assumed to be 0.1m/s (1.25m/s), 0.5K (1.5K), 0.1K (1.5K), and 0.32g/kg (1.5g/kg), respectively. They are used to calculate the error bars, bias, and std in Figure 3. The WS and Ts (or Qs) effects on both sensible and latent heat fluxes are evaluated. Figures 3a and 3b show that sensible heat and latent heat fluxes increase with WS when Ts, Ta, and Qa stay constant. Since Qs varies with Ts, Figures 3c and 3d show that sensible heat and latent heat increase with Ts (or Qs) when WS, Ta, and Qa are kept as baseline values. By varying air temperature (Ta), Figure 3e shows that sensible heat fluxes decrease with increasing Ta (i.e. smaller Ts-Ta difference). Figure 3f reveals that latent heat fluxes decrease with higher Qa (i.e. smaller Qs-Qa) when other parameters are held at baseline values. From these bias and



std, it is concluded that bulk parameterization are more sensitive to temperature and humidity than WS. Based on normalized WS, Qs-Qa difference, and latent heat flux of June-August gridded data, the regression coefficients are 0.75 and 0.52 for WS and Qs-Qa. Applying the same normalization process to WS, Ts-Ta, and sensible heat, the regression coefficients are 0.81 and 0.15 for WS and Ts-Ta. . This means WS is more important factor for latent heat and sensible heat in the Tropics.

Figures 4, 5, and 6 show the occurrence (in percentage) of latent heat with different WS, Qs-Qa difference, and air specific humidity (Qa) based on satellite retrieval of June-August 1998 data. The solid black curves represent the mean latent heat values for the corresponding WS, Qs-Qa difference, and Qa. Latent heat increases with WS (Fig. 4). The most frequent occurrence of wind speed is between 4 and 9m/s in the Tropics, which is the dominant factor for latent heat fluxes in the Tropics. The latent heat also increases with Qs-Qa difference (Fig. 5) with the most occurrence of Qs-Qa difference between 4 and 6g/kg. Figure 6 shows latent heat decreases with Qa. Most tropical surface air is very humid with Qa between 18 to 24 g/kg. Some air with low humidity around 9g/kg is the result of subsidence over relative cooler subtropical regions.

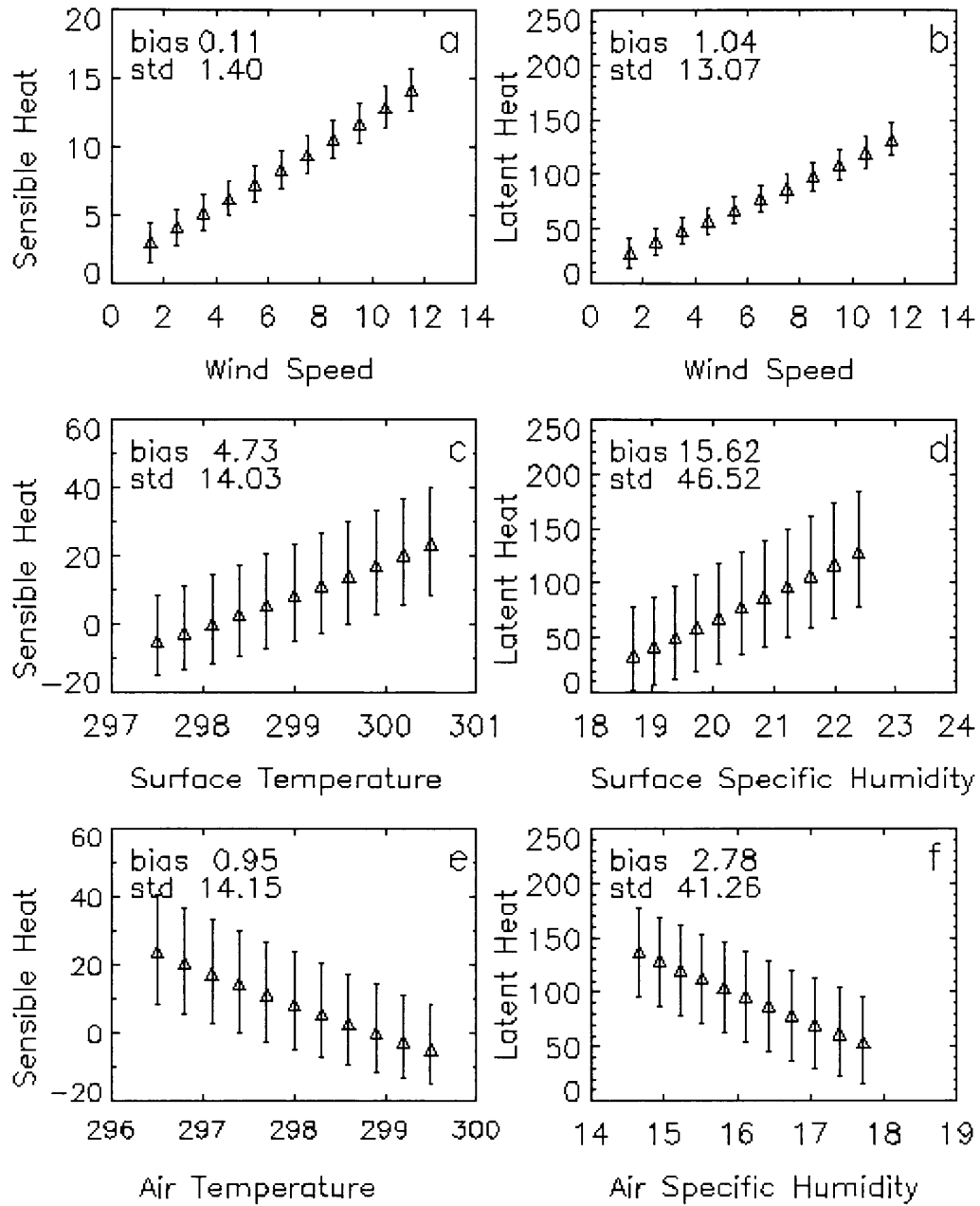


Figure 3. Sensitivity tests of sensible and latent heat fluxes by varying wind speed (m/s), surface temperature (K), and air temperature (K).

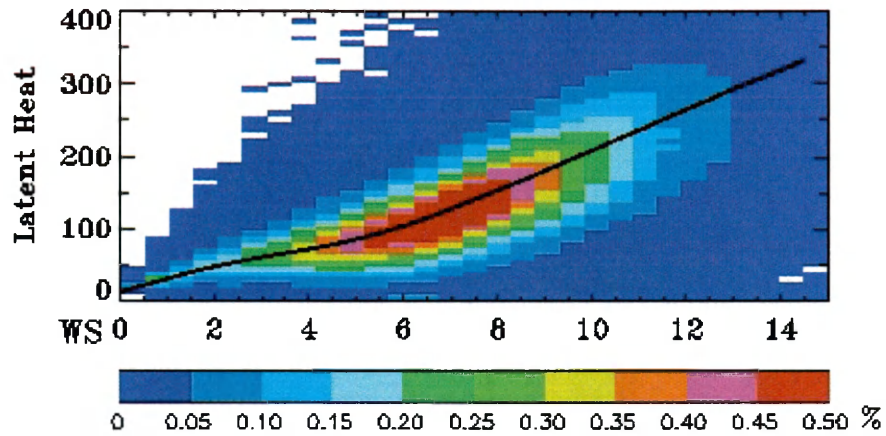


Figure 4. Distribution of latent heat ( $\text{W/m}^2$ ) versus wind speed (m/s) for June – August 1998.

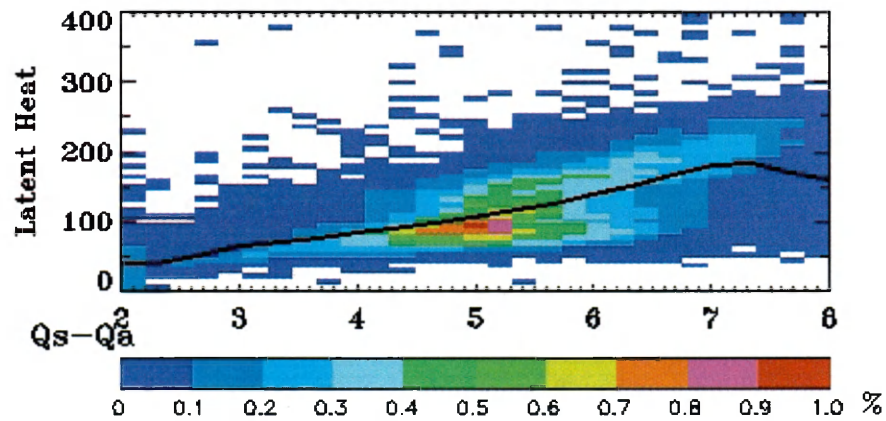


Figure 5. Distribution of latent heat ( $\text{W/m}^2$ ) versus surface and air specific humidity ( $Q_s - Q_a$ ) difference (g/kg) for June – August 1998.

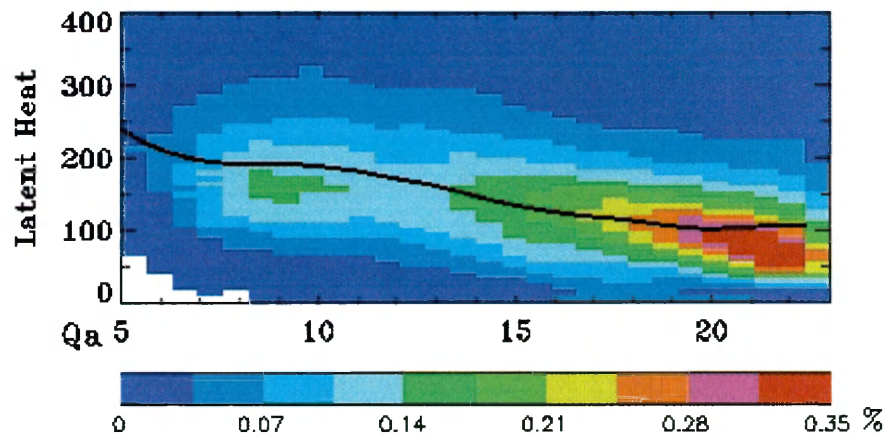


Figure 6. Distribution of latent heat ( $\text{W/m}^2$ ) versus air specific humidity for June–August 1998.

## CHAPTER 4

### VALIDATION AND COMPARISON OF TURBULENT FLUXES

Since the CERES project has extensive studies and validation activities for the derived TOA, surface and within atmosphere SW and LW radiative fluxes, this study concentrates on the validations of sea surface turbulent fluxes and their related satellite retrieved geophysical variables.

#### 4.1 Ship Validation

Comparison of satellite retrievals with ship or buoy ground-truth measurements is required to establish the credibility of the satellite remote sensing. Ship experiments have the advantage of measuring a more comprehensive set of parameters than satellites, but the ship measurements are sparse. There were 5 field experiments conducted by the NOAA Environmental Technology Laboratory (ETL) research ship, R/V Ronald H. Brown, in various legs of its 1999 cruise around the world. They were the Joint Air-Sea Monsoon Interaction Experiment (JASMINE), the Nauru 99 (NAURU99), the Kwajalein Experiment (KWAJEX), the Pan-American Climate Study (PACSF99), and the buoy service in the North Pacific (MOORINGS) which is the only one sailed into middle latitudes ( $49^{\circ}\text{N}$ ). The other four legs were all within  $12^{\circ}\text{S}$  to  $13^{\circ}\text{N}$ . Each experiment lasted approximately one month. The ETL cruise measured radiation and turbulent fluxes, and bulk meteorological variables. There are three values produced from ship measurements for latent and sensible heat fluxes. The first two are calculated using direct covariance (COV) and the inertial-dissipation (ID) methods. The third one is calculated using ship measured meteorological variables and the COARE bulk algorithm. NAURU99 conducted during June 15 to July 18, 1999, is used for comparison in this study.

Because of temporal and spatial differences between ship and TMI measurements, it is possible to have multiple TMI pixels for a single ship measurement. The TMI pixels

were collocated with each of the NAURU99 ten-minute measurements to be within 10 minutes and 20 km. Although there are 4764 NAURU99 measurements available, only 66 measurements were found to have matched TMI pixels. These matched TMI pixels were run through the COARE algorithm (Fariall et al. 1996) using satellite estimated temperatures, humidities, and wind speeds. The satellite estimated fluxes for each pixel were averaged into the 66 NAURU99 measurements, and compared to the ship results from COV, ID, and COARE bulk algorithms. Figures 7a and 7b show that the bias and rms errors between satellite estimation and ship measurements are -0.06m/s and 1.05m/s for wind speed, and -0.44K and 1.46K for surface temperature, respectively. The wind speed rms error (1.05m/s in Fig. 7a) is smaller than those from SSM/I (~2m/s by Goodberlet et al. and ~1.4m/s by Schluessel et al.). Figures 7c and 7d show that the bias and rms are 0.32g/kg and 1.44g/kg for air specific humidity, and -0.07K and 1.46K for air temperature. The bias and rms are 1.91W/m<sup>2</sup> and 40.88W/m<sup>2</sup> for latent heat (Fig. 7e), and -1.64W/m<sup>2</sup> and 6.30W/m<sup>2</sup> for sensible heat (Fig. 7f). The comparison of GSSTF-2 input variables with tropical field experiments based on daily means has a bias (rms) of 0.36 (1.43)m/s, -0.47 (0.94) K, and 0.67 (1.40)g/kg for wind speed, surface temperature, and air specific humidity. They have a bias (rms) of 0.8 (35.7)W/m<sup>2</sup> and 6.4 (12.0)W/m<sup>2</sup> for latent heat and sensible heat, respectively, (Chou 2003). Kano and Kubota (2000) compared J-OFURO with in-situ data and estimated the rms to be 40 and 20W/m<sup>2</sup> for three-day and monthly means, respectively. Comparisons with in-situ measurements show that the algorithm used in this study provides results with similar or less uncertainty than those from SSM/I and other remote sensing microwave measurements.

Table 2 shows the results of latent heat from satellite retrieval and from three ship-based estimates (COV, ID, and bulk algorithms). The diagonal displays mean values (99.57, 101.48, 108.01, 113.94W/m<sup>2</sup>). The upper right part of the table shows the correlations between these algorithms, and the lower left part shows the bias and rms (in parenthesis) errors. It can be seen that the latent heat of TMITF only have an instantaneous bias and rms errors of -1.91W/m<sup>2</sup> and 40.88W/m<sup>2</sup>, when compared to ship COV measurements. The negative sign means TMITF underestimate. The main sources

of uncertainty are the  $Q_a$  and wind speed estimation in satellite retrieval and the ship motion, flow distortion, and the contaminating effects of the marine environment in the ship measurements. The limited sample size and, spatial and temporal mismatch in collocated data also contribute to bias and rms errors. Note that compared with the COV estimate, the latent heat fluxes retrieved directly from ship measurements of  $WS$ ,  $T_s-T_a$ , and  $Q_s-Q_a$  by COARE bulk formula have larger bias errors than the satellite estimate ( $-12.46 \text{ W/m}^2$  vs  $-1.91 \text{ W/m}^2$  in tables 2), indicating the gridded mean values of the satellite data may have significantly smaller errors than the instantaneous data. The validation of sensible heat in the Tropics gets less attention, partly because of its small value and also because of the inadequate accuracy of air temperature derived from satellite data. However, sensible heat loss is not negligible, especially at higher latitudes. Table 3 shows the results of sensible heat from satellite estimation and ship measurements. The TMITF underestimates sensible heat by  $1.64 \text{ W/m}^2$  when compared to ship COV estimates.

Table 2. Latent heat statistics from satellite bulk estimation and ship (COV, ID, and bulk) measurements. Means in diagonal, correlation coefficients in upper right corner, and bias and rms (in parenthesis) in the lower left corner.

	Satellite Bulk	Ship Covariance	Ship inertial-dissipation	Ship bulk
Satellite bulk	<b>99.57 <math>\text{W/m}^2</math></b>	0.142	0.333	0.506
Ship Covariance	-1.91 (40.88)	<b>101.48 <math>\text{W/m}^2</math></b>	0.542	0.604
Ship inertial-dissipation	-8.47 (49.45)	-6.53 (43.04)	<b>108.01 <math>\text{W/m}^2</math></b>	0.665
Ship bulk	-14.37 (30.79)	-12.46 (29.39)	-5.93 (38.38)	<b>113.94 <math>\text{W/m}^2</math></b>

Table 3. Sensible heat statistics from satellite bulk estimation and ship (COV, ID, and bulk) measurements. Means in diagonal, correlation coefficients in upper right corner, and bias and rms (in parenthesis) in the lower left corner.

	Satellite Bulk	Ship Covariance	Ship inertial-dissipation	Ship bulk
Satellite bulk	<b>3.08 <math>\text{W/m}^2</math></b>	0.106	0.050	0.372
Ship Covariance	-1.64 (6.31 )	<b>4.72 <math>\text{W/m}^2</math></b>	0.450	0.584
Ship inertial-dissipation	-2.57 (8.58)	-0.93 (7.55)	<b>5.65 <math>\text{W/m}^2</math></b>	0.243
Ship bulk	-1.02 (3.98)	0.62 (4.30)	1.55 (7.55)	<b>4.10 <math>\text{W/m}^2</math></b>

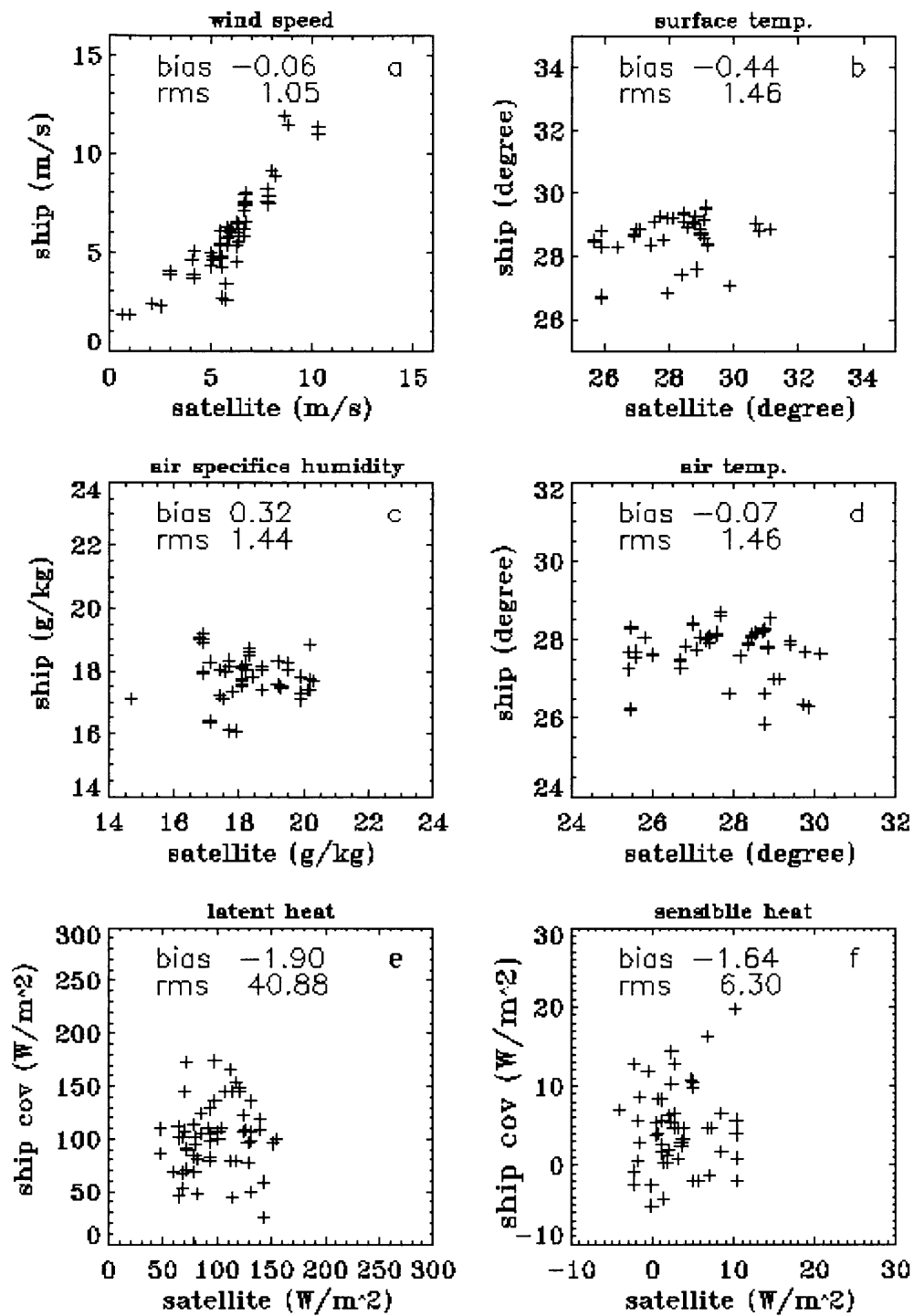


Figure 7. Satellite estimates versus ship (NAURU99) measurements.

## 4.2 Satellite Comparison

The TMITF turbulent fluxes are compared to the GSSTF-2 products produced by the surface turbulent fluxes research group at NASA Goddard, led by Dr. Shu-Hsien Chou. This data set covers from July 1987 through December 2000, and is retrieved from the data collected by Special Sensor Microwave Imager (SSM/I) onboard Defense Meteorological Satellite Program (DMSP) satellites F-8, F-10, F-11, F-13, and F-14. These DMSP satellites fly in sun-synchronous orbits. The SSM/I instruments measure brightness temperature at four frequencies 19.35, 22.235, 37.0, and 85.5GHz. The key differences between TMI and SSM/I are the additional pair of horizontally and vertically polarized 10.65GHz channels and a frequency change of the water vapor channel from 22.235 to 21.3GHz in TMI. The change off the center of the water vapor line in TMI was made to avoid the absorption saturation of water vapor for the TRMM tropical orbit. The polarized 10.65GHz channels are used in the retrievals of wind speed and sea surface temperature. The resolutions of GSSTF-2 are daily and monthly means for global oceans in  $1^\circ$  by  $1^\circ$  grid boxes. Therefore, TMITF measurements were averaged into monthly gridded values for comparison.

Both TMITF and GSSTF-2 use bulk algorithms to estimate air-sea interface turbulent fluxes with the same input parameters: sea surface temperature ( $T_s$ ), air temperature ( $T_a$ ), surface specific humidity ( $Q_s$ ), air specific humidity ( $Q_a$ ), and wind speed ( $WS$ ). The reference height of  $T_a$ ,  $Q_a$ , and  $WS$  is set to 10 m for TMITF, while GSSTF-2 use 10 m for  $WS$  and  $Q_a$  and 2m for  $T_a$ . GSSTF-2 uses daily mean values of these input parameters to calculate the daily fluxes. The daily mean wind speeds and water vapor amounts are from Wentz (1997), while surface and air temperatures and surface pressure are from NCEP reanalysis.  $Q_s$  is calculated based on daily means of surface temperature and pressure. TMITF calculates wind speeds, air specific humidity, and surface temperatures using TMI BT measurements as explained in previous sections, and estimates air temperatures by applying the temperature difference between surface



and air temperatures of ECMWF to the estimated surface temperatures. TMITF uses instantaneous values of these parameters to calculate the fluxes and then averages them into hourly, daily, and monthly means.

To estimate the air specific humidity ( $Q_a$ ), GSSTF-2 uses the two-step method of Schulz et al. (1993), which estimates the water content of the lowest 500 meter layer ( $W_{500}$ ) from total column water vapor, and then relates  $Q_a$  to  $W_{500}$ . TMITF uses the optimized one-step method of Schluessel et al. (1995), which directly retrieves  $Q_a$  from the measured brightness temperatures. The accuracies for these two methods are comparable, approximately 1.2g/kg and 1.1g/kg for two-step and one-step methods, respectively (Schluessel 1997). The saturated specific humidity at the surface ( $Q_s$ ) of GSSTF-2 is determined from the daily mean sea surface temperature and sea-level pressure of NCEP reanalysis. The  $Q_s$  values of TMITF, on the other hand, are calculated with concurrent sea surface temperature and a fixed surface pressure of 1013.25mb. Both consider a 2% reduction in the saturated vapor pressure for saline water as compared to pure water.

Although there are many differences in the source and retrieval methods of input parameters between TMITF and GSSTF-2, the monthly zonal and gridded results are generally in good agreement between these two data sets. Figures 8 and 9 show the zonal and gridded averages of latent heat fluxes of TMITF and GSSTF-2. The values range from approximately 50 to 200W/m<sup>2</sup> for zonal mean and 0 to 300W/m<sup>2</sup> for gridded mean. They are correlated well between 20°N and 20°S, although the TMI values are lower than those from SSM/I by 3 to 15W/m<sup>2</sup>. At latitudes higher than 20°, TMI flux values are higher than those from SSM/I by 6 to 17W/m<sup>2</sup> because of higher wind speed estimations in TMITF. The monthly averaged latent heat differences for entire tropical oceans are -6.6, -3.2, -2.9, -2.0, -7.2, 1.1, 2.9, and -2.4W/m<sup>2</sup> for the first eight months of 1998. Figures 10 and 11 show the zonal and gridded averages for sensible heat. Zonal means range from 0 to 15W/m<sup>2</sup> for TMITF, which are lower than those from SSM/I across all compared latitudes by 6-7W/m<sup>2</sup>. Chou et al. (2003) found that GSSTF-2 has a positive bias of 7W/m<sup>2</sup> due to underestimates of air temperature in NCEP. Both TMITF and

GSSTF-2 maps show that the winter hemisphere has higher latent heat and sensible heat fluxes than the summer hemisphere due to the shifts of the trade winds with the season.

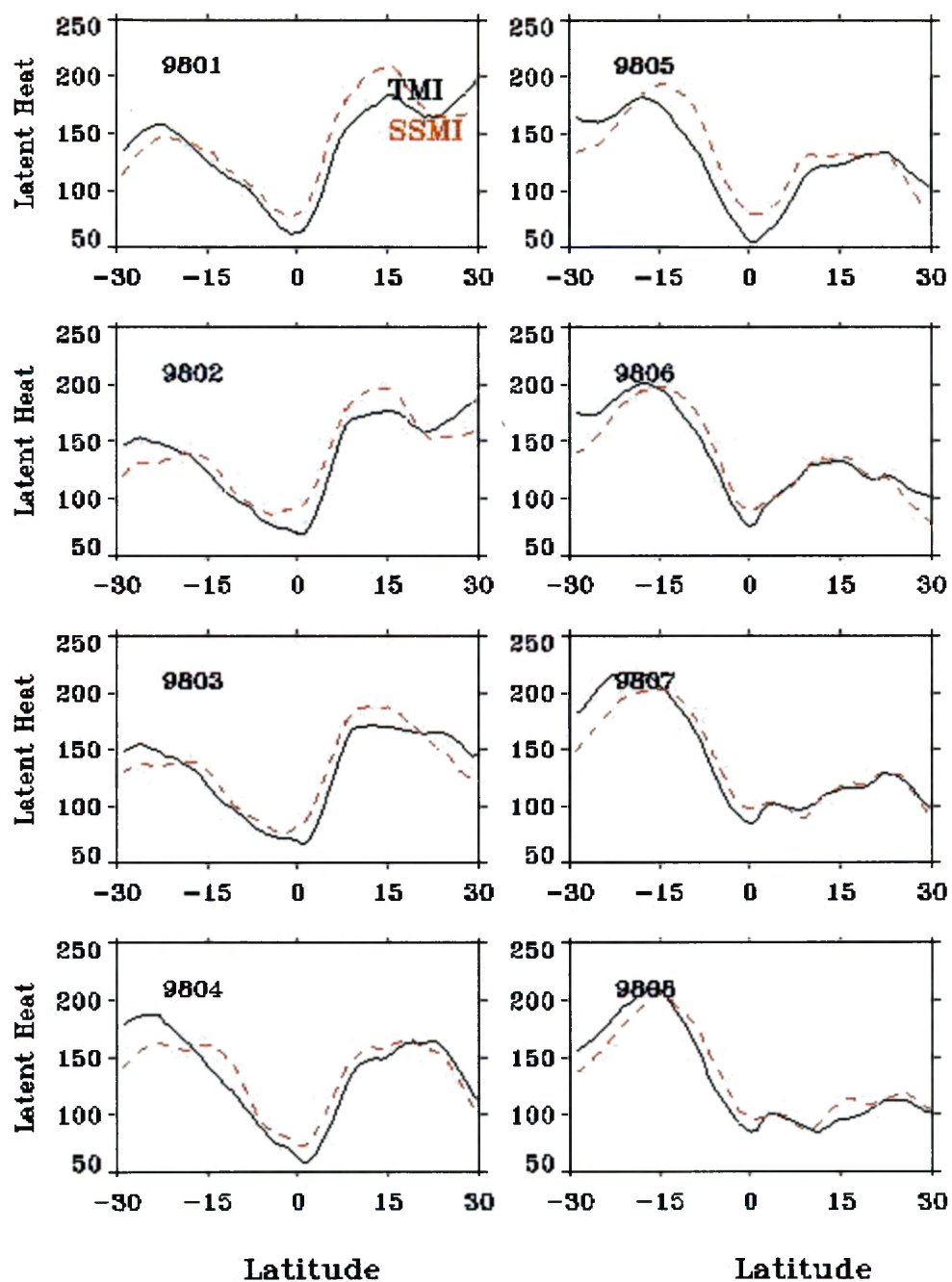


Figure 8. Zonal averages of latent heat flux for TMI (solid line) and SSM/I (dashed line).

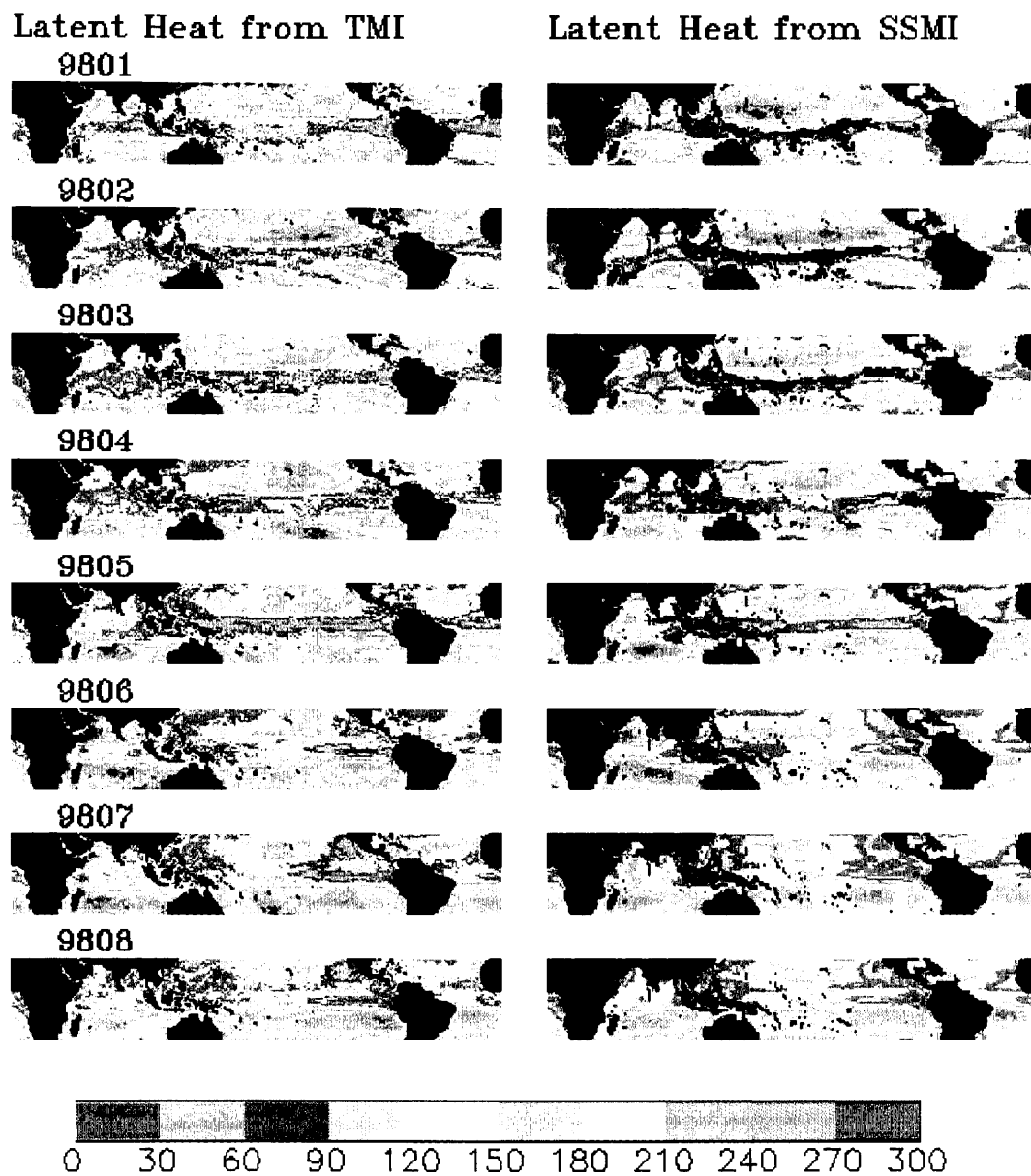


Figure 9. Gridded averages of latent heat flux for TMI and SSM/I.  
(The black stripes along the equator for SSM/I is due to the lack of data)

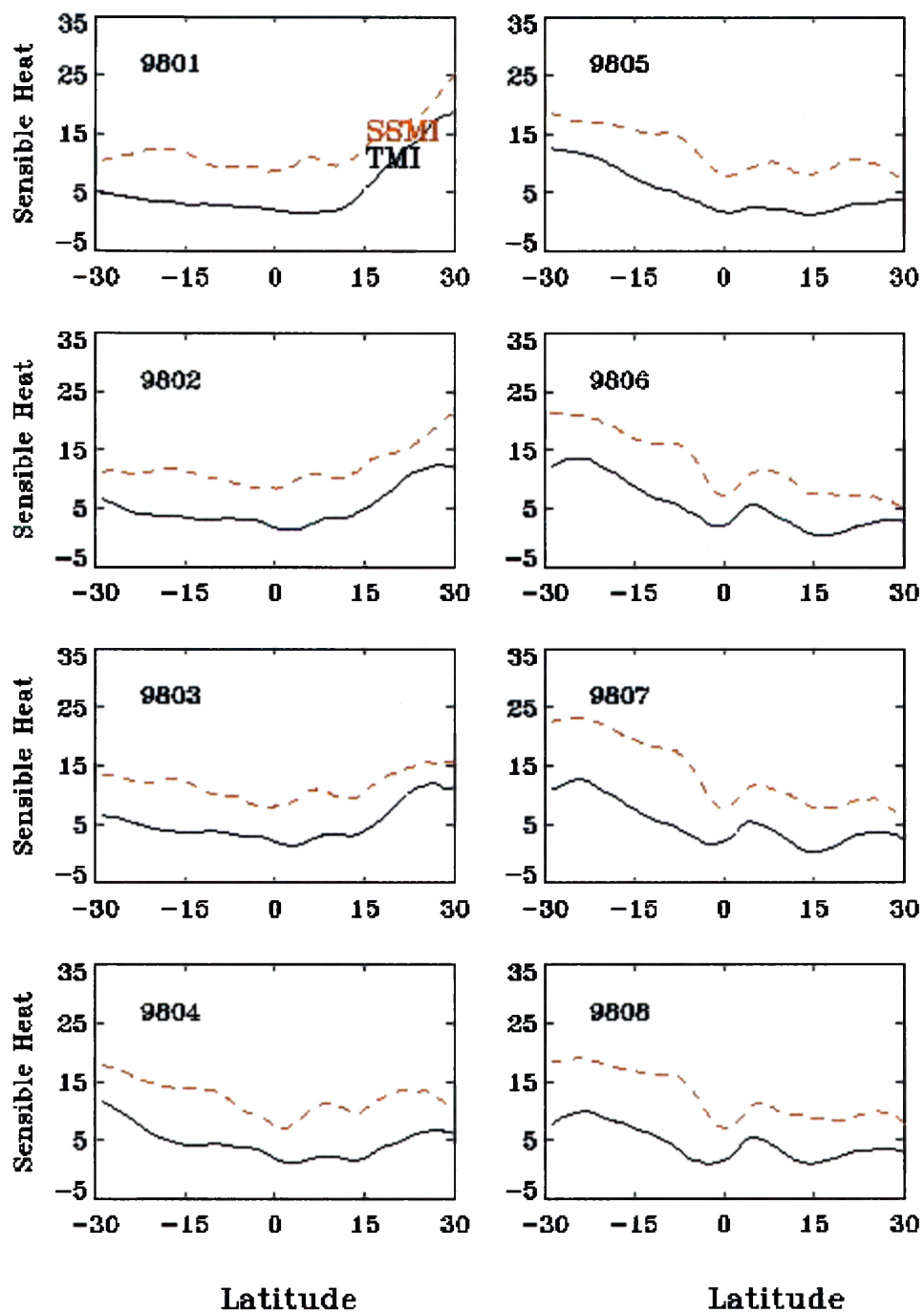


Figure 10. Zonal averages of sensible heat flux for TMI (solid line) and SSM/I (dashed line).

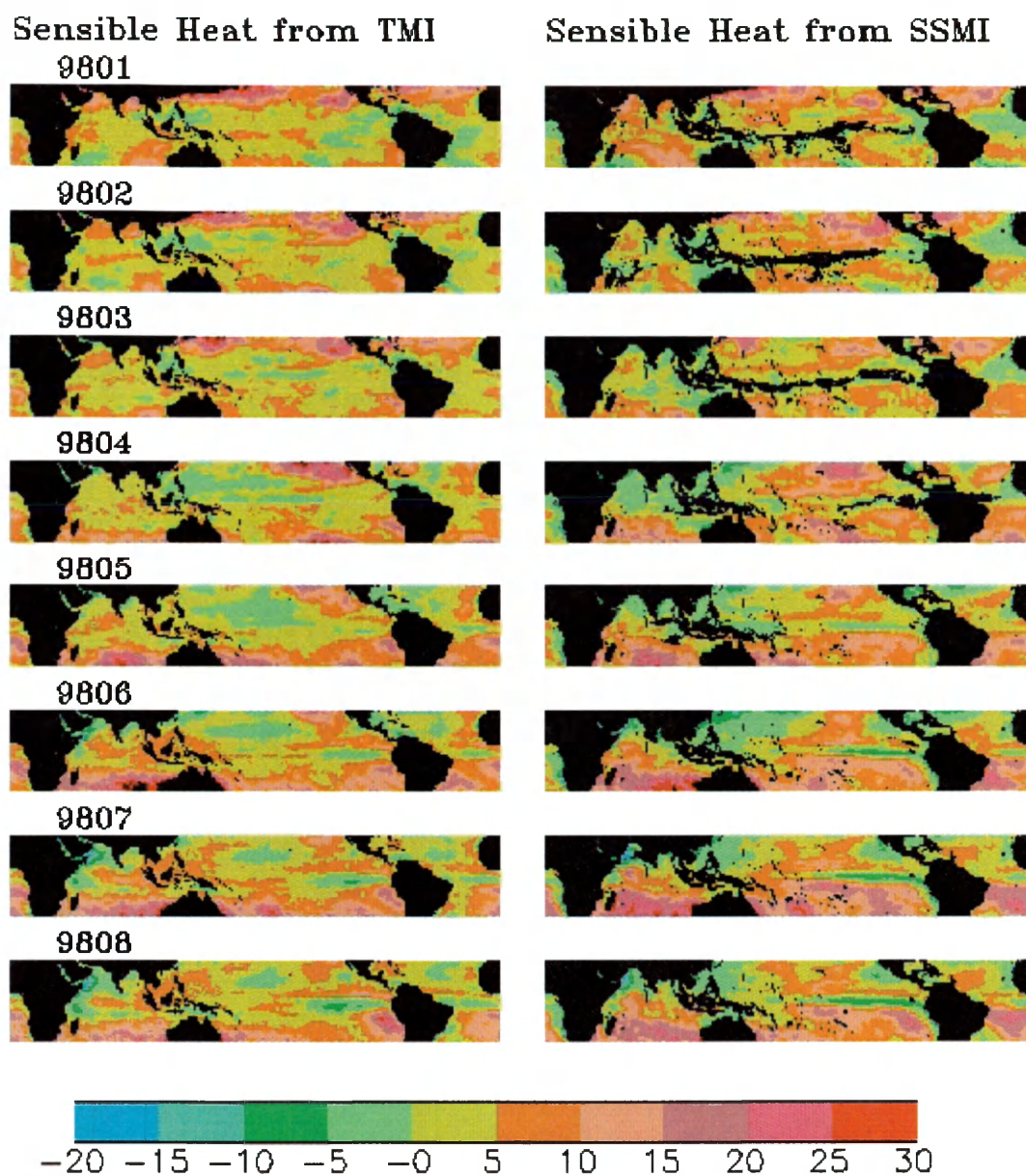


Figure 11. Gridded averages of sensible heat flux for TMI and SSM/I.  
(The black stripes along the equator for SSM/I is due to the lack of data)

## CHAPTER 5

### NET SURFACE FLUXES

This chapter starts with discussions of the major parameters that influence the heat fluxes and their geographical distribution and diurnal variation, and ends with the estimated net surface fluxes. Radiative SW and LW fluxes from TRMM CERES are available for the first eight months of 1998, therefore the net surface fluxes (NSF) gained by oceans in  $1^\circ$  by  $1^\circ$  grids and latitudinal zones for these eight months are calculated for hourly, monthly, and seasonal means. The pictures to be discussed hereafter use color bars with positive and negative values to represent heat gain and loss by oceans, respectively.

#### 5.1 Shortwave Radiation

Figure 12 shows the net SW fluxes for three seasons (winter, spring, and summer for northern hemisphere). The gridded net surface SW varies from 50 to  $350\text{W/m}^2$  and is highest along  $20^\circ$  latitudinal zones in the summer hemisphere because of more insolation and less clouds. The lower net SW values are at higher latitudes in the winter hemisphere. Since SW radiation comes from the solar insolation, the strongest shortwave fluxes occur during noontime, and there is no SW flux during nighttime. The colorful boxes in Figure 13 show the occurrence (in percentage) of net surface SW fluxes for each hour based on June-August 1998 data. It reveals that SW fluxes are at least  $200\text{W/m}^2$  and can reach  $900\text{W/m}^2$  during noon hours. The solid black curve shows the hourly means of net surface SW radiation over the tropical oceans ( $30^\circ\text{S}$ - $30^\circ\text{N}$ ).

#### 5.2 Longwave Radiation

Net surface LW fluxes vary from  $-100$  to  $0\text{W/m}^2$  (Fig. 14). The least amount of LW loss occurs at the equator where heavy clouds and humid boundary layer absorb



upwelling LW radiation and re-emit most of it back to the surface. The cold tongue off the west coast of South America is evident by its low net LW values, especially in the southern hemisphere winter time.

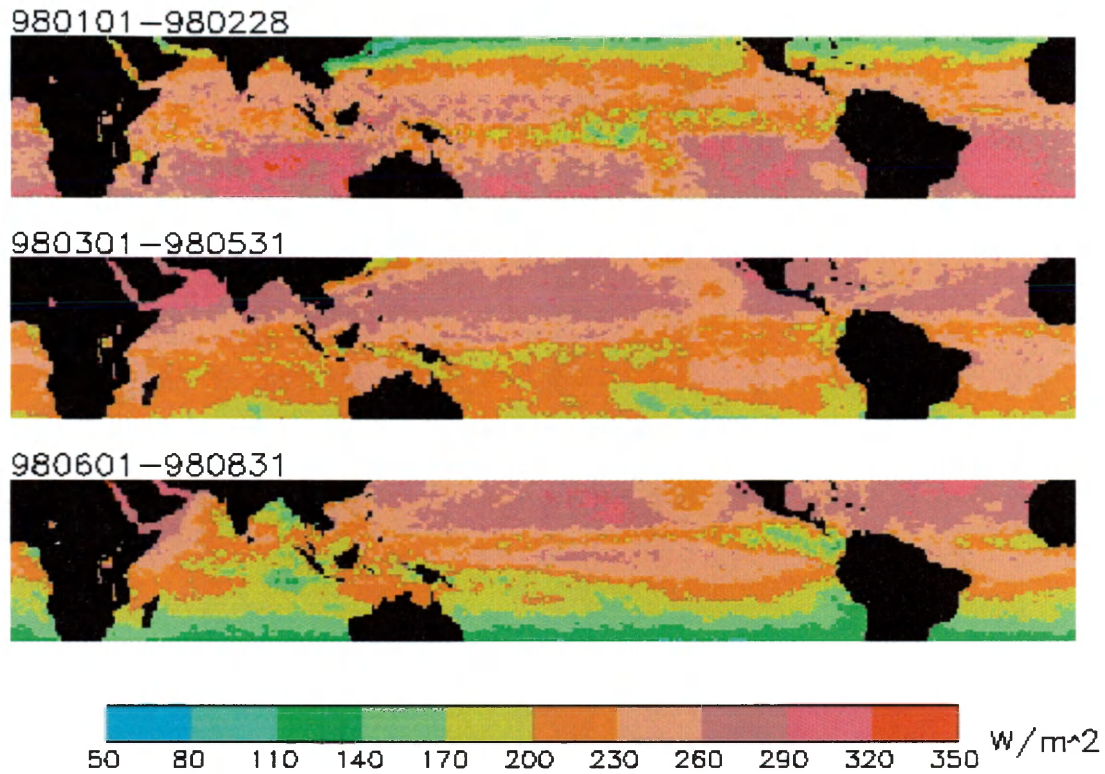


Figure 12. Estimation of net surface shortwave fluxes from TRMM.

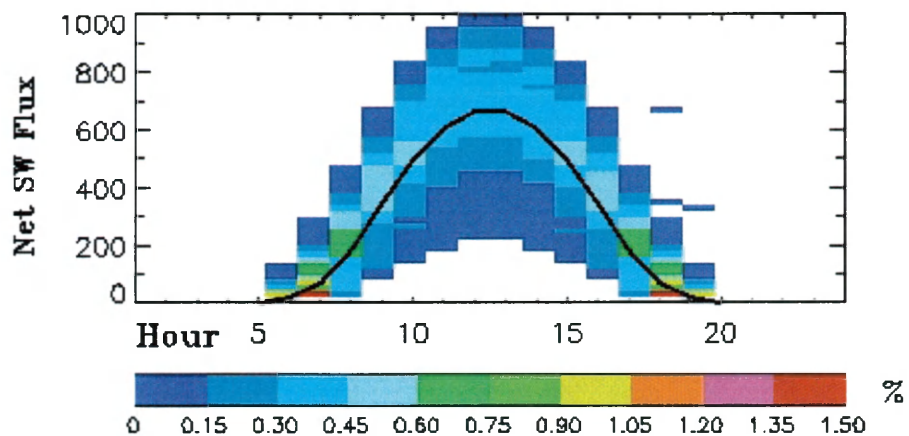


Figure 13. Occurrence (%) and diurnal variation of net surface shortwave fluxes ( $\text{W/m}^2$ ) from TRMM for June-August 1998.



Both net SW and LW fluxes have lower values along the ITCZ and SPCZ because there are more convective clouds, which reflect incoming SW and block outgoing LW radiation. The occurrences (in percentage) of net surface LW fluxes for each hour based on June-August 1998 data are plotted in Figure 15 for entire tropical oceans ( $30^{\circ}\text{S}$ - $30^{\circ}\text{N}$ ). Most LW flux loss ranges between 20 and  $60\text{W}/\text{m}^2$ , although some can lose as much as  $100\text{W}/\text{m}^2$ . The black solid curve is the hourly means. The diurnal variation is not significant in this picture because of small LW diurnal variability, but it is clearly shown in Figure 16. The net LW heat loss is higher in the afternoon than in the early morning by about  $5\text{W}/\text{m}^2$ , because the surface temperature is higher after absorbing the SW from the Sun during daytime hours.

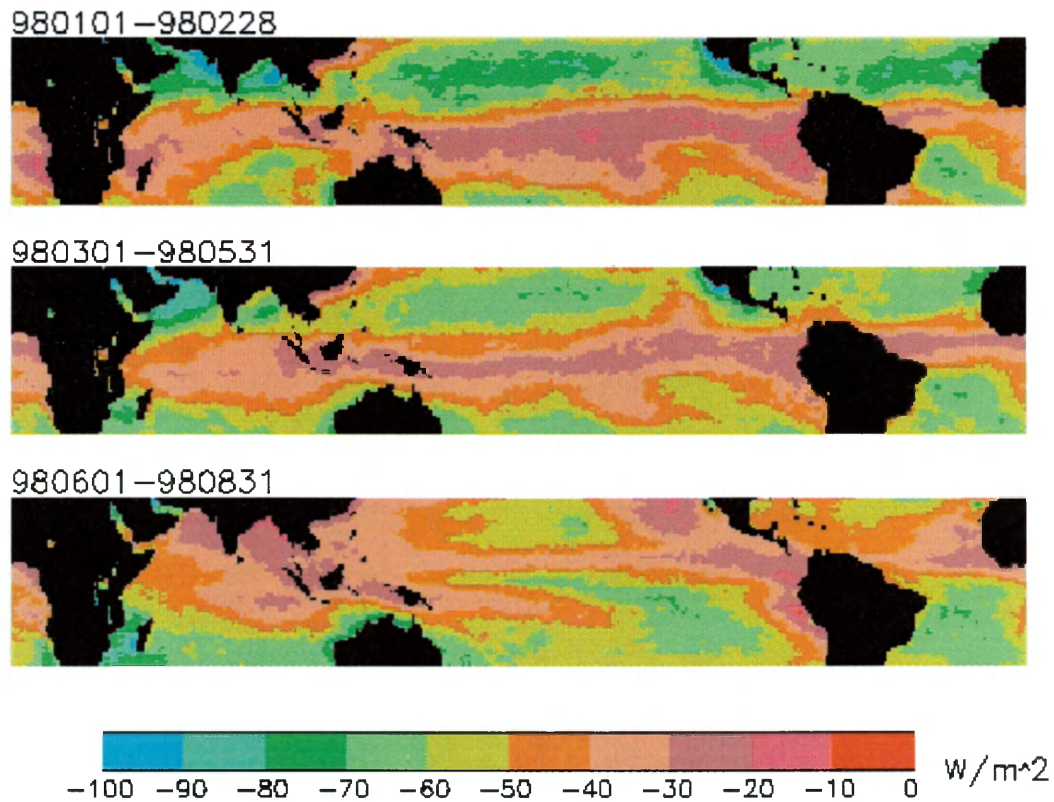


Figure 14. Estimation of net surface longwave fluxes from TRMM.

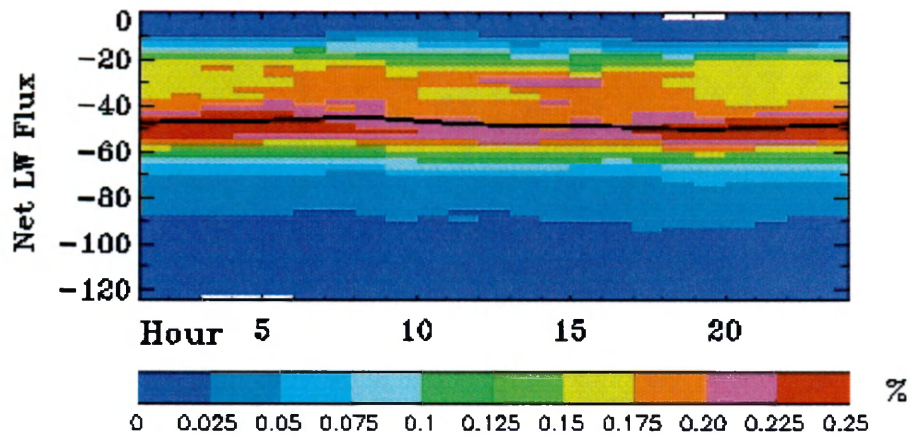


Figure 15. Occurrence (%) and diurnal variation of net surface LW fluxes ( $\text{W/m}^2$ ) from TRMM for June-August 1998.

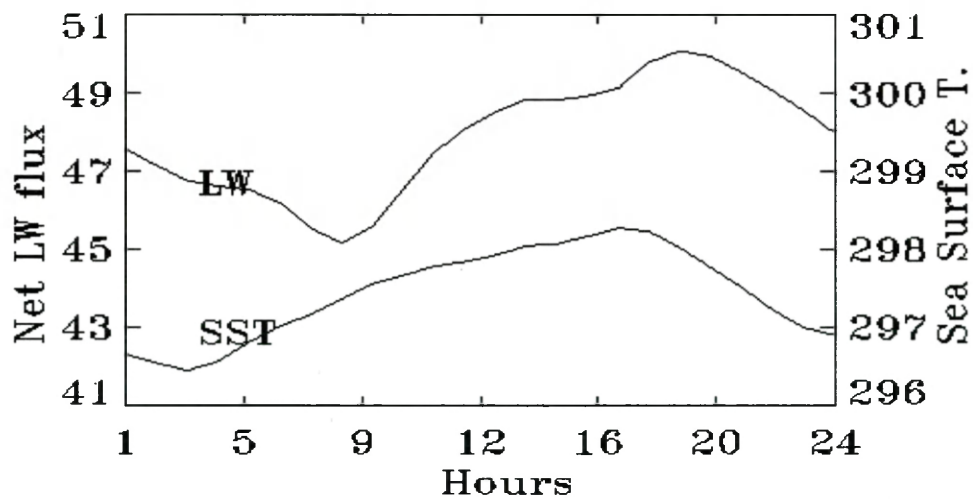


Figure 16. Diurnal variation of net surface longwave fluxes ( $\text{W/m}^2$ ) from TRMM for June-August 1998.

### 5.3 Wind Speed

Winds in the tropical region usually blow from east to west. Mesoscale wind fields can be extremely intense with circular vortices called tropical cyclones. Most of these storms develop during the summer season over eastern and western Pacific, western Atlantic, and Indian oceans. They are the strongest surface winds observed in the earth's atmosphere. Besides tropical cyclones, winds are usually higher at the trade wind zones and extra-tropical storm tracks. They are lower at the ITCZ, SPCZ, and tropical Indian ocean. The gridded seasonal averages are shown in Figure 17. During June-August, equatorial western and eastern Pacific areas have the lowest wind speeds. The winter

hemisphere usually has higher winds. Based on June-August 1998 data, wind speeds are lower in the afternoon hours than those in the morning hours (red curve in Fig. 24).

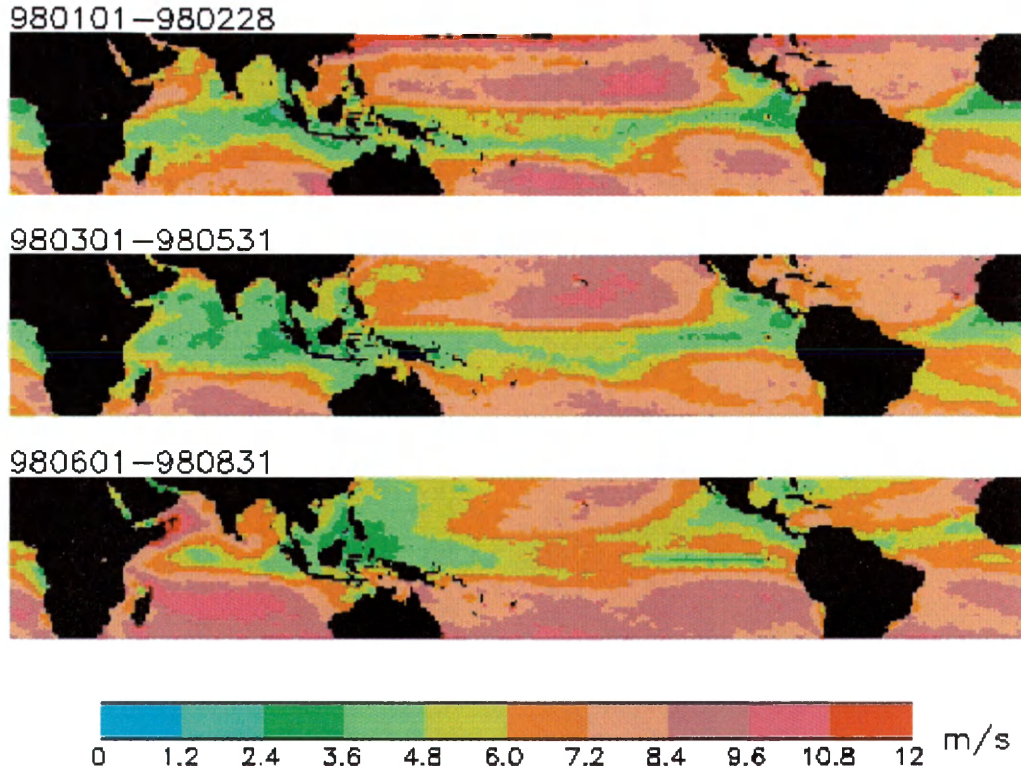


Figure 17. Wind speed (m/s) distribution from TRMM satellite.

#### 5.4 Humidity

Figures 18 and 19 display the surface and air specific humidity ( $Q_s$  and  $Q_a$ ) distributions. Higher  $Q_s$  values are along the equator and western Pacific and Atlantic oceans, while lower  $Q_s$  values are located in the winter hemisphere. This distribution is a reflection of sea surface temperature (Fig. 25).  $Q_a$  has similar distribution as  $Q_s$ , but with smaller values. The difference between these two humidities is shown in Figure 20. The least humidity difference is along the equator and eastern Pacific oceans. Winter hemisphere has larger humidity differences than summer hemisphere, because of slower decrease of  $T_s$  than  $T_a$  and strong influence of the nonlinear relationship between saturation humidity and temperature decided by Clausius-Clapeyron equation. Figure 21 shows the diurnal variations of  $Q_s$ ,  $Q_a$ , and  $Q_s - Q_a$ . Afternoon



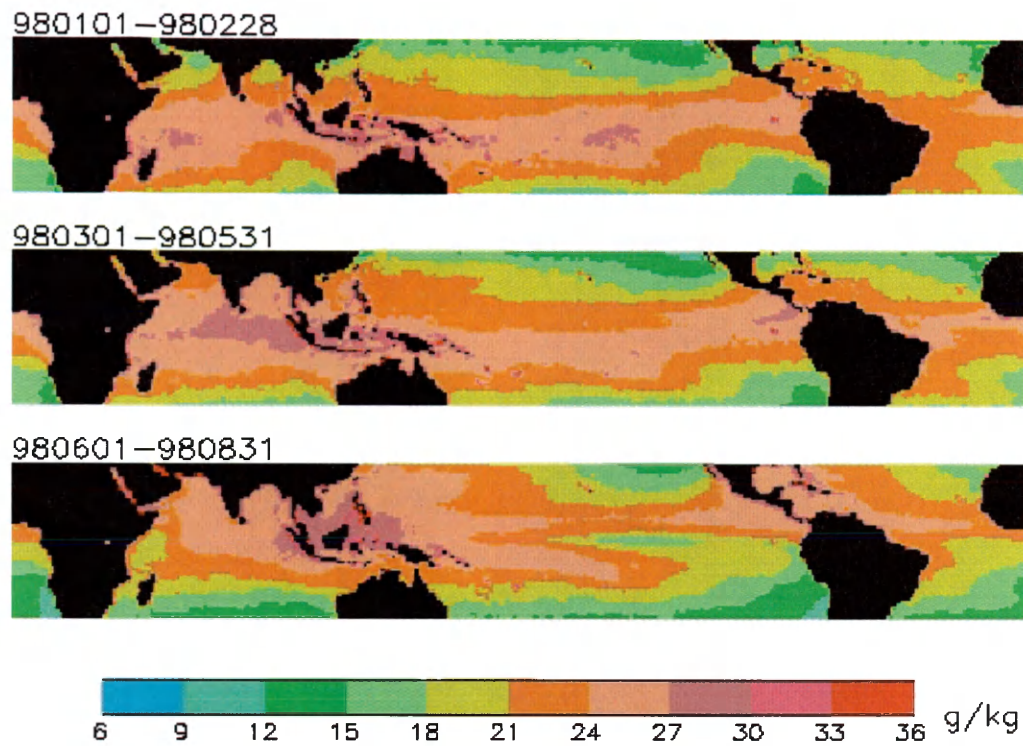


Figure 18. Surface specific humidity ( $Q_s$ ) distribution from TRMM.

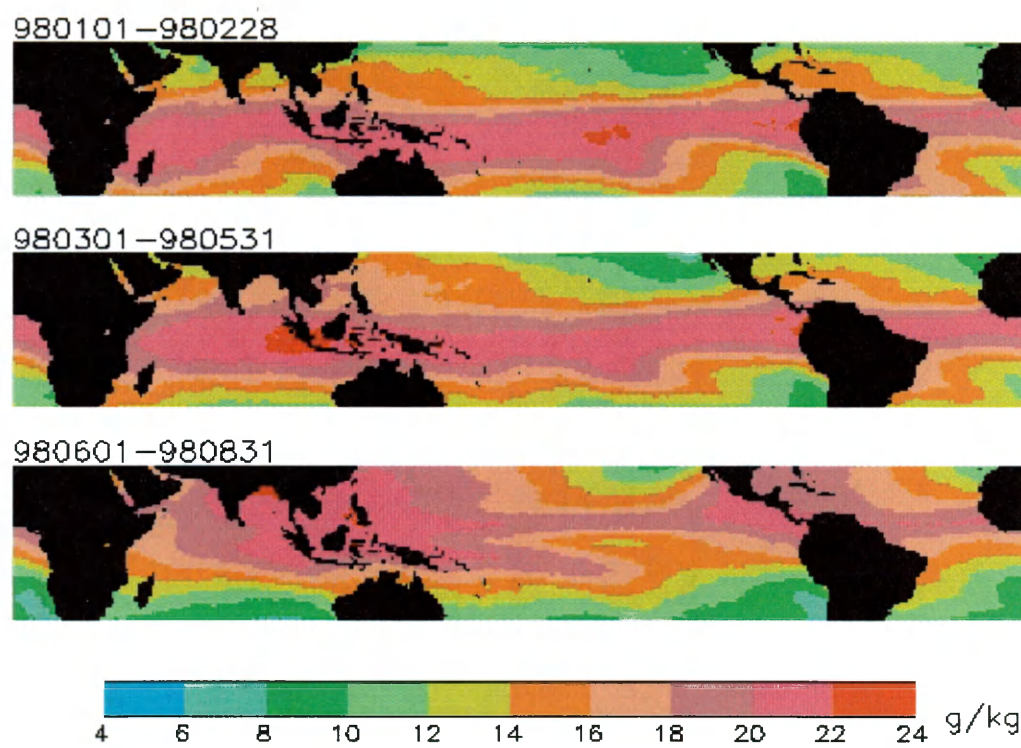
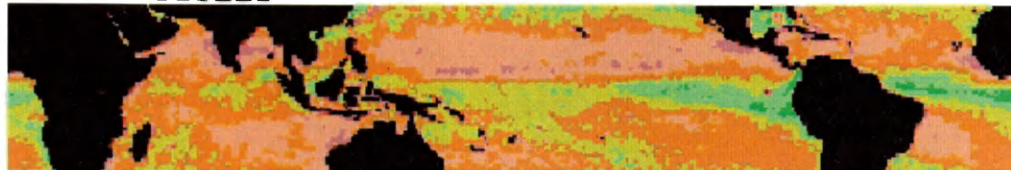


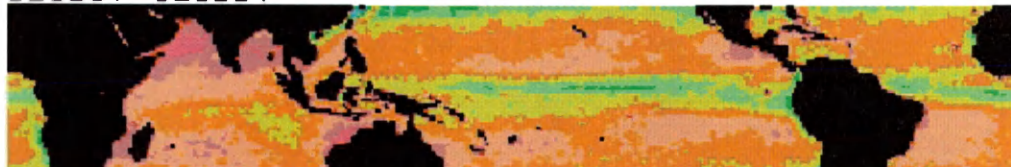
Figure 19. Air specific humidity ( $Q_a$ ) distribution from TRMM.

hours (noon to 8PM) have higher  $Q_s$ - $Q_a$  differences than morning or night time hours.

980101–980228



980301–980531



980601–980831

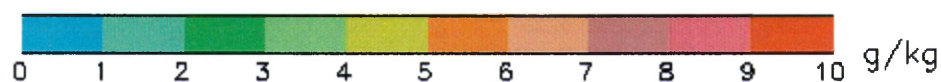
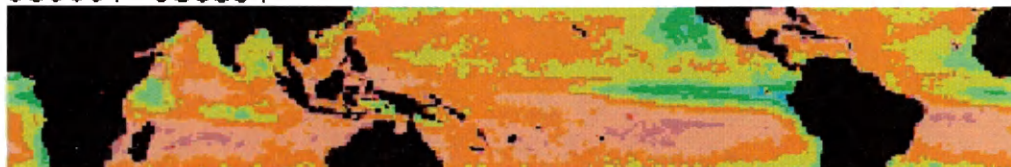


Figure 20. Surface and air specific humidity difference ( $Q_s - Q_a$ ) from TRMM.

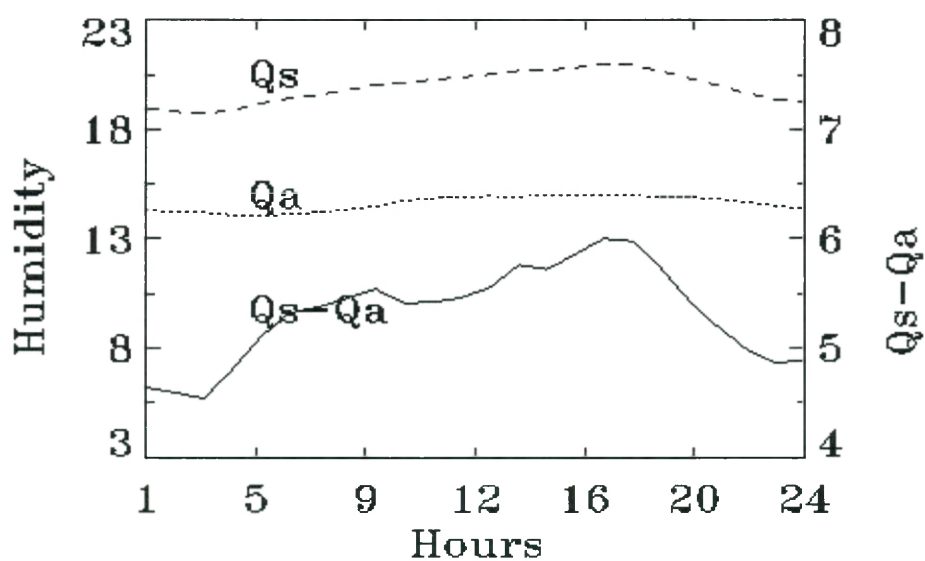


Figure 21. Diurnal variation of surface and air humidity (g/kg) from TRMM for June-August 1998.

### 5.5 Latent Heat Fluxes

Figure 22 shows that latent heat (LH) fluxes, varying from  $-300$  to  $0 \text{ W/m}^2$ , generally have small absolute values at the equator and along the ITCZ and SPCZ due to low wind speeds (Fig. 17) and high boundary layer humidity (Fig. 19) (i.e. small  $Q_s - Q_a$  differences in Fig. 20). The convective zones have upwelling-induced cold sea surface temperature and weak winds. The smallest LH losses ( $< 30 \text{ W/m}^2$ , red color in Fig. 22) correspond to the lowest  $Q_s - Q_a$  area (green in Fig. 20). The other smaller LH fluxes are observed in the western and eastern Pacific ocean where warm humid air is dominant and leads to minimal moisture transport from ocean to the atmosphere. LH loss is generally higher in the winter hemisphere, especially between  $15^\circ$  and  $20^\circ$  latitudes due to higher wind speeds and lower air humidity (i.e. higher humidity difference). The LH distribution in Fig. 22 clearly shows the effects of wind speeds. It indicates that wind speed may play a dominant role in the Tropics, while the humidity difference may be the dominant factor in extra-tropical regions. Figures 23 shows that most LH losses are between  $50$  to  $150 \text{ W/m}^2$ . For diurnal variation, there are two peaks shown in Figure 24, one in the early

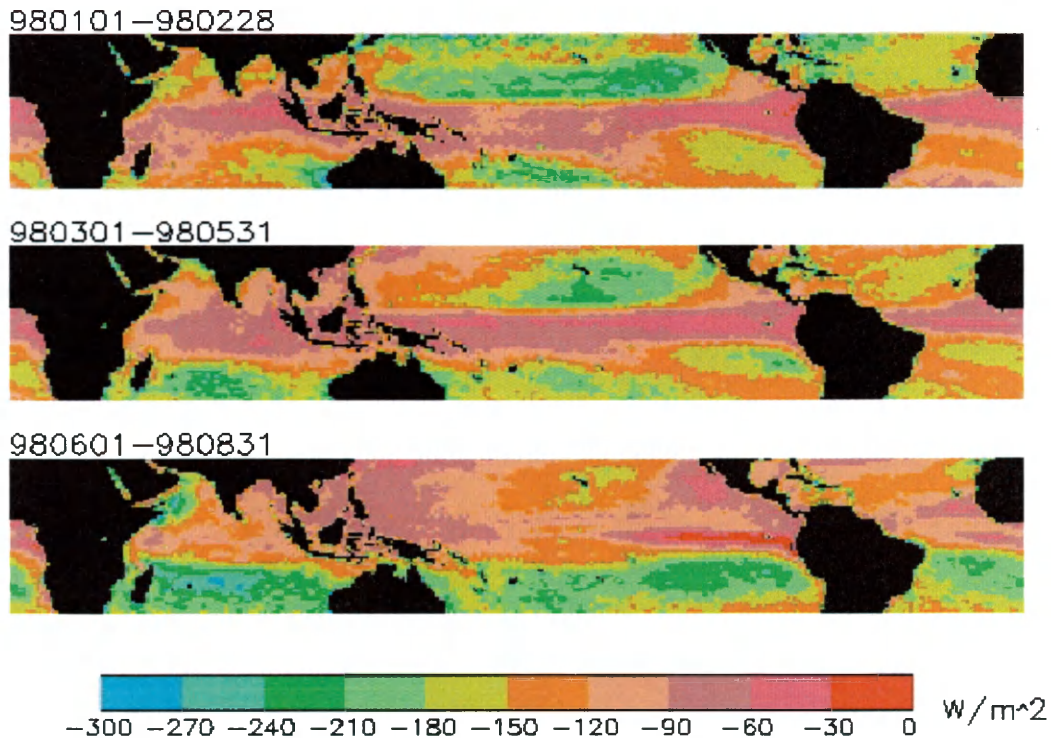


Figure 22. Estimation of latent heat fluxes from TRMM.



morning hours and the other in the late afternoon. The peak at 7p.m. has the highest LH loss. A minimal LH loss coincides with the lowest wind speed at 1p.m.. The least LH loss occurs at ~5 a.m., which can be related to the maximum wind convergent period over tropical oceans. Following the double peaks of tropical oceanic convection, the boundary layer is generally drier than before the convection (or moist static energy is lower), which causes the LH peaks in the diurnal variations.

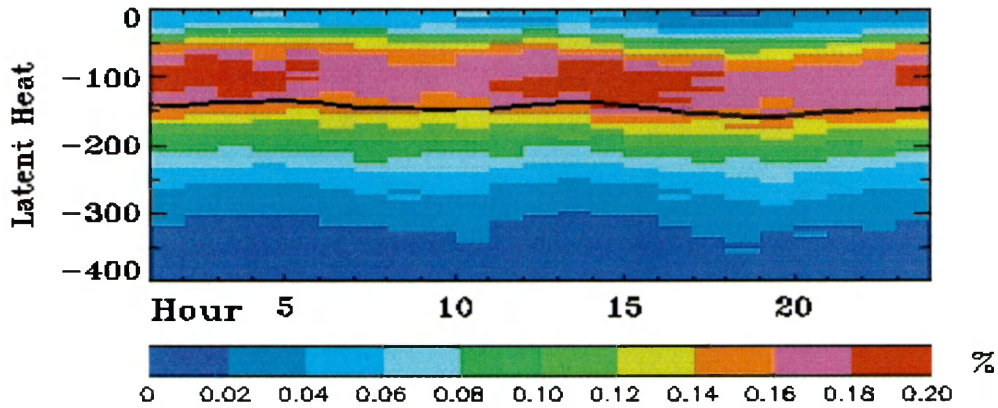


Figure 23. Occurrence (%) and diurnal distribution of latent heat fluxes ( $\text{W/m}^2$ ) from TRMM for June-August 1998.

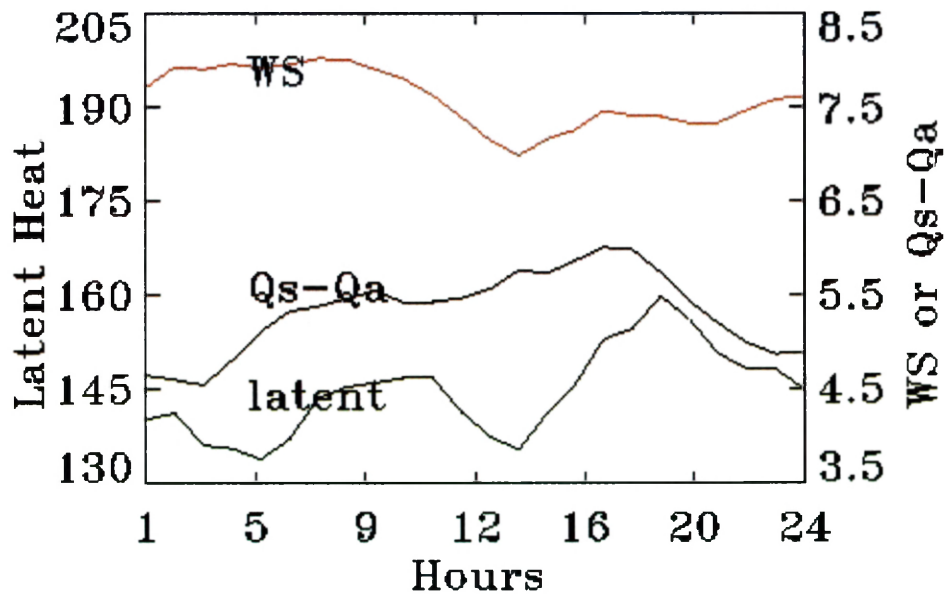


Figure 24. Diurnal variations of latent heat fluxes ( $\text{W/m}^2$ ), wind speed (m/s), and  $Q_s - Q_a$  (g/kg) from TRMM for June-August 1998.

## 5.6 Sensible Heat Fluxes

The sea surface temperature (Ts) estimated from TRMM and surface-air temperature differences from ECMWF are plotted in Figures 25 and 26. Ts is higher along the ITCZ and SPCZ, and over Indian and tropical western Pacific oceans. The Ts-Ta differences vary mostly between  $-0.5\text{K}$  and  $1.5\text{K}$  except for the area higher than  $20^\circ$  in the winter hemisphere, where it can be more than  $3\text{K}$  and have higher heat losses. The calculated sensible heat fluxes range from  $-8$  to  $32\text{W/m}^2$ , therefore the color bars are from  $-32$  to  $8\text{W/m}^2$  to indicate the heat losses from surface to the atmosphere in Fig. 27. From figures 17, 26, and 27, it can be seen that both WS and Ts-Ta difference are important factors for the sensible heat fluxes. Figure 28 shows the diurnal variations of sensible heat fluxes. Generally, the variations of sensible heat fluxes follow the changes of WS with significant modifications from the surface-air temperature differences.

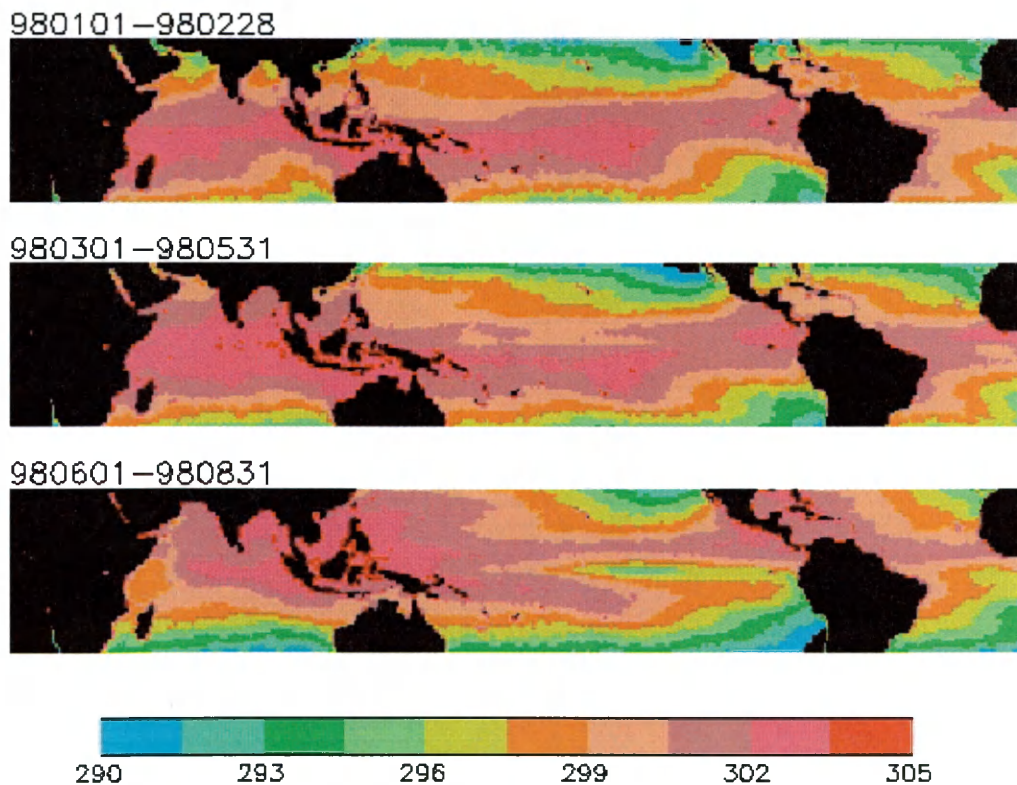
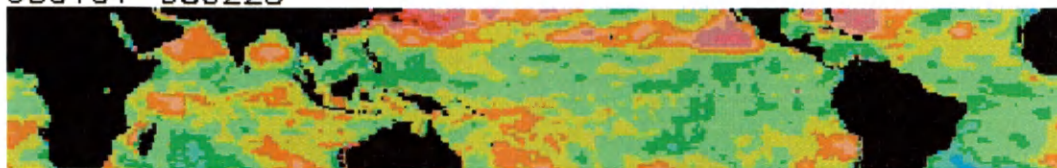


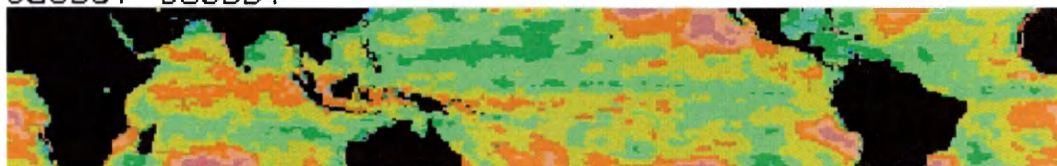
Figure 25. Estimation of sea surface temperature from TRMM.



980101–980228



980301–980531



980601–980831

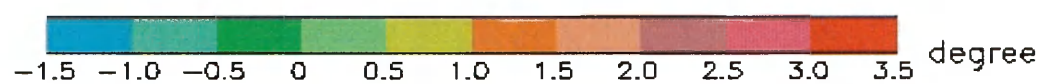
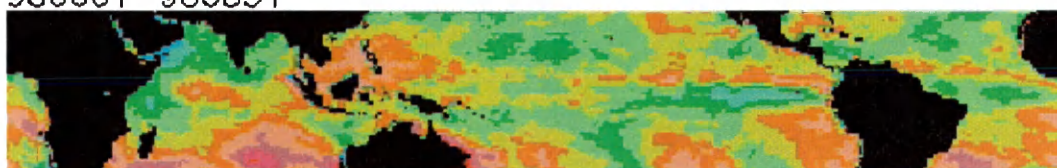
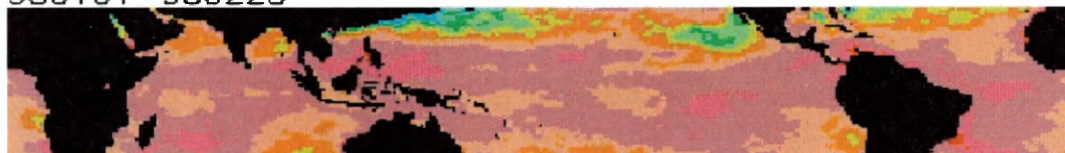
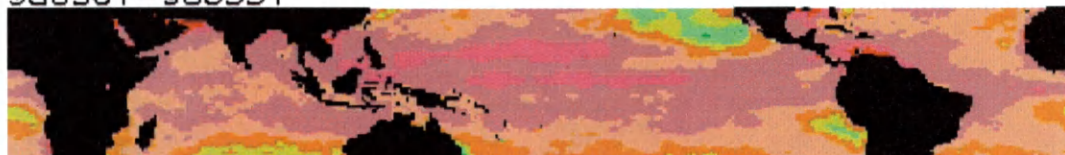


Figure 26. Surface and air ( $T_s - T_a$ ) temperature differences from ECMWF.

980101–980228



980301–980531



980601–980831

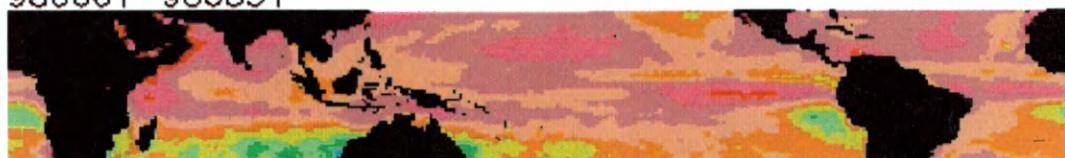


Figure 27. Estimation of sensible heat fluxes from TRMM.

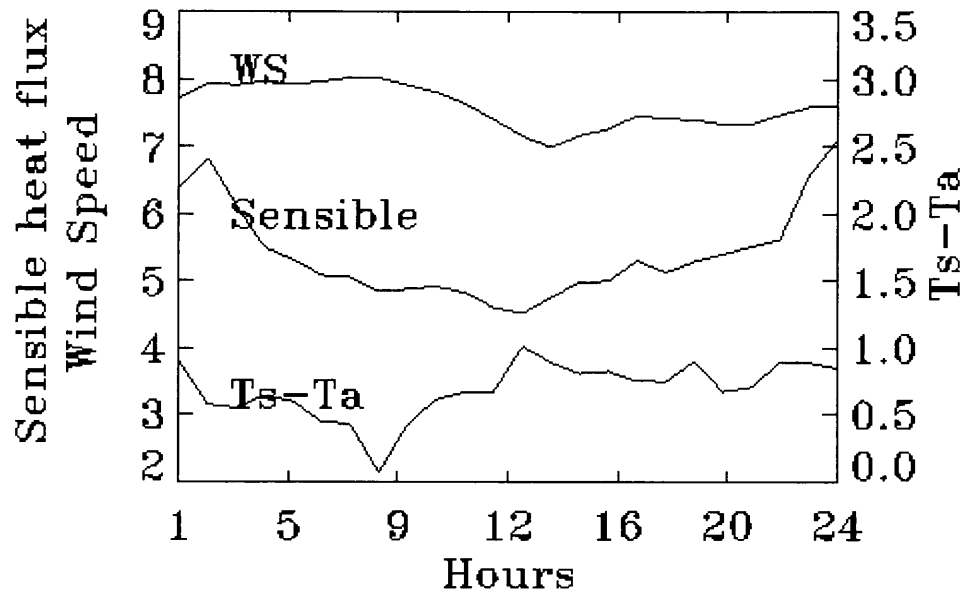


Figure 28. Diurnal variation of sensible heat fluxes ( $\text{W/m}^2$ ) and wind speed ( $\text{m/s}$ ) from TRMM, and  $T_s - T_a$  from ECMWF for June-August 1998.

### 5.7 Net Surface Fluxes

Previous sections have shown that the global distributions of estimated heat components are strongly related to the atmospheric general circulation. The seasonal and diurnal variations of the fluxes are mainly the results of changes in the solar insolation, temperature, dynamics, and convection. All of the components are added together and Figure 29 shows the net surface fluxes (NSF) for the three seasons available in gridded means. The values vary between  $-250$  and  $250 \text{ W/m}^2$ . The oceans gain heat from the atmosphere (or actually from the Sun) during the summer months, and lose heat to the atmosphere during wintertime. The highest heat gain is along the equator year round because of high gains in SW and low losses in LW fluxes. Generally, the NSF has the same pattern as net SW fluxes with modifications from latent heat fluxes (Figures 12, 22, 29), especially for the convergence, subsidence, and storm track regions. This indicates that LH and SW fluxes are not only important for the surface energy budget but also are the dominant factors in driving the atmosphere general circulation. Figure 30 shows the

diurnal variations of net surface fluxes. There are net heat losses during night hours (6p.m. to 6a.m.) and net heat gain during daytime hours with the highest heat gain at noon time over the Tropics. The black curve is similar to the net surface SW curve in Fig. 13 except  $\sim 200\text{W/m}^2$  lower. The zonal means for each heat flux component and the net surface flux are plotted in Fig. 31. The solid black, red, green, and blue curves represent net SW, net LW, turbulent latent, and turbulent sensible heat fluxes, respectively. The rain-induced sensible heat is very small in zonal averages. If plotted in this figure, it would be very close to the blue line due to the big scale used here and is therefore omitted from this picture. Finally, the broad dashed curve shows the NSF amounts. It is obvious that, the summer hemisphere gains more SW fluxes and the winter hemisphere losses more LW and latent heat fluxes. The NSF stays at  $50\text{-}100\text{W/m}^2$  in summer hemisphere and drops from approximate  $100\text{W/m}^2$  at equator to approximate  $-100\text{W/m}^2$  at  $30^\circ$  in the winter hemisphere. The net NSF is negative at regions higher than  $15^\circ$  in the winter hemisphere. This transition of heat gain and loss for oceans is highly related to the insolation or the seasonal variation of the Earth's climate. Total NSF over the tropical regions is positive because of maximum solar radiation. The positive tropical total NSF is generally balanced by the loss of fluxes at higher latitudes. Table 4 summarizes the seasonal flux means for the entire tropical ocean ( $30^\circ\text{S} - 30^\circ\text{N}$ ).

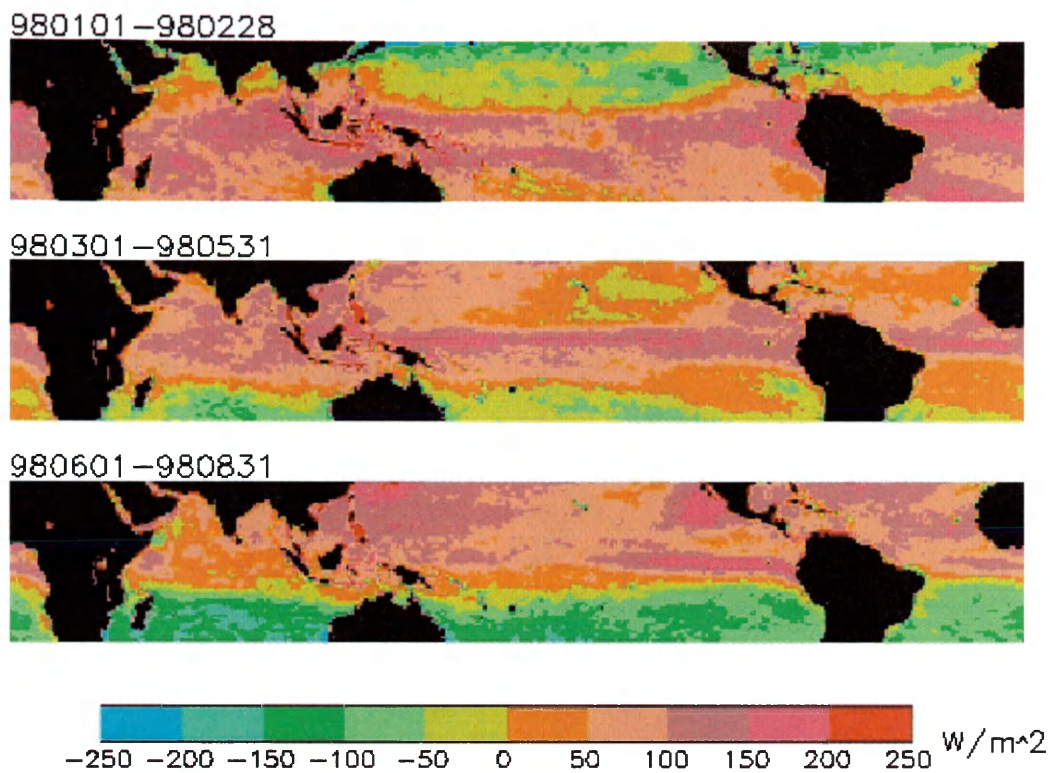


Figure 29. Estimation of net surface fluxes from TRMM.

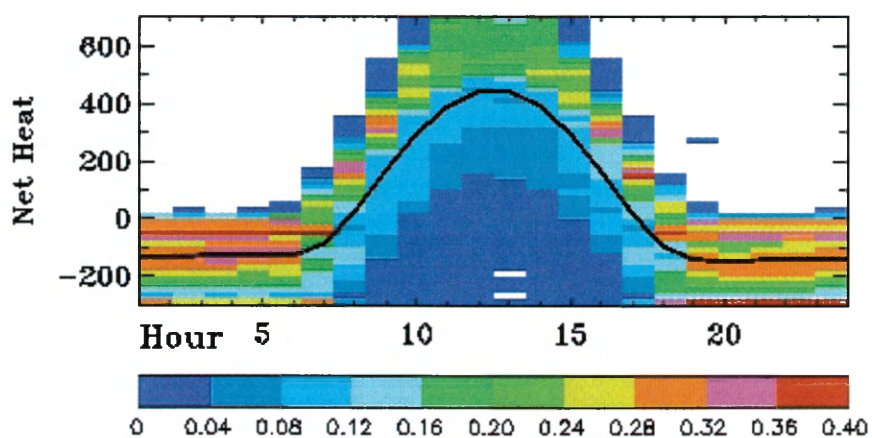
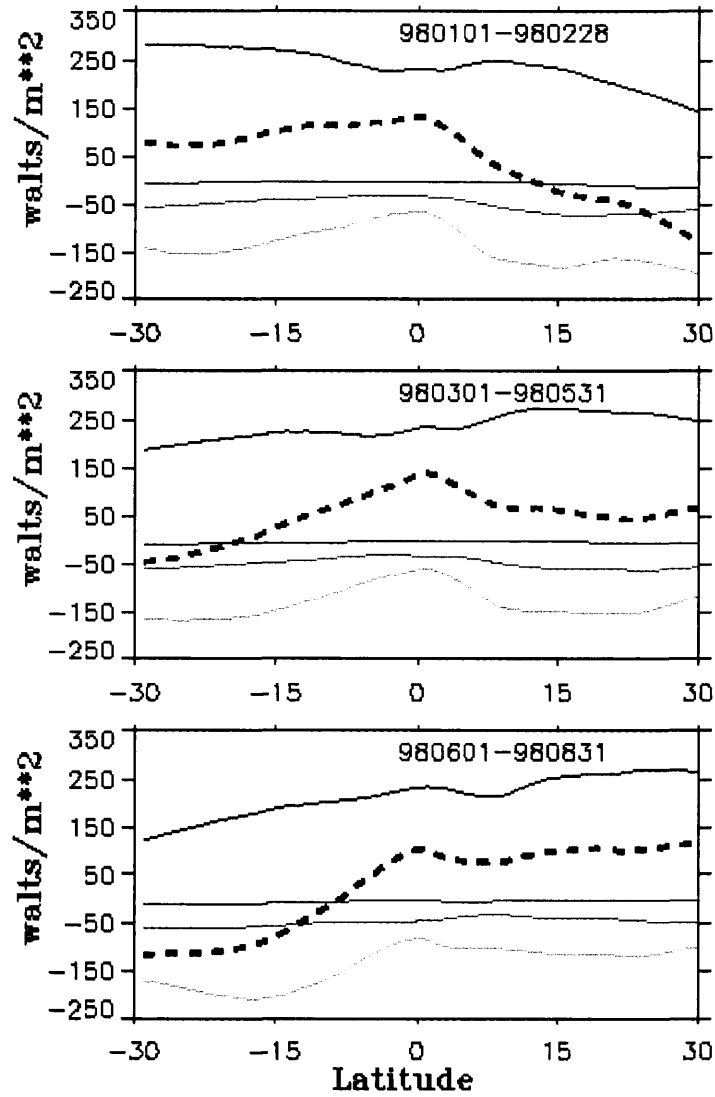


Figure 30. Occurrence (%) and diurnal distribution of net surface heat fluxes ( $\text{W/m}^2$ ) from TRMM for June-August 1998.



{Net SW    Net LW    Latent heat    Sensible Heat }

Figure 31. Zonal mean estimation of surface net fluxes (dashed line) from TRMM.

Table 4. Seasonal mean for shortwave, longwave, latent, sensible, and net surface heat fluxes for tropical ocean (30°S – 30°N).

	shortwave	longwave	latent	sensible	net
980101-980218	239.6	-49.5	-137.0	-5.0	53.3
980301-980531	234.9	-49.1	-131.4	-4.7	54.7
980601-980831	213.2	-47.2	-139.89	-5.2	26.2

## CHAPTER 6

### SUMMARY AND CONCLUSION

The importance of air-sea interaction in the atmosphere-ocean coupled system is widely appreciated. The role of the tropical oceans for climate variation in inter-annual and longer time scales cannot be overstated. The existing global scale flux data sets are limited to certain components of surface fluxes. There have been no comprehensive net surface flux data sets which consider all major heat components for the tropical oceans or for large spatial scale distributions. Good estimates of the major heat components with global coverage are useful for the validation of ocean and coupled atmosphere-ocean models. TRMM is the first satellite providing the opportunity to estimate radiation, latent and sensible heat, and rain-induced sensible heat fluxes simultaneously, using instruments onboard the same satellite and covering the entire Tropics. An integrated approach to determine these heat flux components and net surface heat fluxes over the tropical oceans is studied in this paper.

The radiative heat fluxes are strongly affected by cloud properties. The turbulent heat fluxes are mainly correlated with atmospheric dynamics and thermodynamics, especially wind speed and humidity and temperature differences at sea surface and near-sea surface levels. These properties have strong variations on small temporal and spatial scales. Only satellite-based observations can provide a comprehensive estimate of these parameters. The accuracy of satellite sensed latent and sensible heat is limited by the accuracy of air temperature, humidity, and wind speed estimates and the bulk algorithms. The current microwave technique may be less accurate under high wind situations than in normal conditions and cannot retrieve wind speed and air humidity under precipitating clouds.

Besides the input parameters, the drag transport coefficients in the bulk formula are important factors for achieving high accuracy. The COARE bulk algorithm, used by many turbulent flux data sets, has been fine-tuned to the tropical warm pool region, which generally has low winds ( $< 10$  m/s). The lack of ground measurements by ship or buoy at

high latitudes and under strong wind conditions makes it difficult to validate the turbulent flux results at those regions. Therefore, the new version COARE algorithm (version 3.0, 2003) needs further investigation over high latitude areas. Based on this study, the turbulent sensible heat is an order of magnitude smaller than the latent heat over the tropical oceans. The rain-induced sensible heat is about two orders of magnitude smaller than the latent heat, but rainfall's instantaneous cooling of the ocean surface and the increase of the buoyancy flux at sea surface water is not negligible. Although it is beyond the scope of this study, it is important to investigate the rain-induced sensible heat over the oceans during intensive convective events.

Since the TRMM satellite has a precessing orbit, different days may have different observational (or overpass) times for each region. With its swath of ~760 km and 90 minutes per orbit, TRMM cannot cover the whole Tropics in an hour. This means that for a specific hour, only small portion of the Tropics has the data. It takes 46 days for TRMM to come back to the same local time of equator crossing. It is only suitable to use the averages of at least 46-day cycle to study the spatial or temporal variations. TMITF is the only flux data set available for the study of episodic events and diurnal cycle variations. Based on June-August gridded data, surface-air humidity and temperature differences, net LW, and latent heat losses are higher in the afternoon. The sensible heat loss is higher in the evening because of higher WS. CERES provides an unprecedented accuracy for radiation fluxes at TOA and surface. TMITF provides the estimates of turbulent fluxes based on state of the art techniques of retrieving wind speed, humidity, and surface temperature. Combining both products, the temporal resolution of net surface fluxes covers from hourly to daily, monthly, and seasonal averages are drawn in this study. The analysis of these values for the first eight months of 1998, in general, is consistent with the current understanding of monthly and seasonal surface heat flux variations. Although TRMM is designed for precipitation sciences, this study expands it to an entirely new research area. This study also can be easily applied to Aqua satellite that basically has all the VIRS, CERES, and TMI channels used in this study.



## Reference

Charlock, T, F. Rose, D. Rutan, and Q. Fu, 2000: Retrievals of the surface and atmospheric radiation budget for January 1998, International Radiation Symposium 2000.

Chou, M.- D., W. Zhao, S.-H. Chou, 1998: Radiation budgets and cloud radiative forcing in the Pacific warm pool during TOGA COARE. *J. Geophys. Res.*, 103, 16967-16977

Chou, S.-H., W. Zhao, and M.-D. Chou, 2000: Surface heat budgets and sea surface temperature in the Pacific warm pool during TOGA COARE. *J. Climate*, 13, 634-649.

Chou, S.-H., E. Nelkin, J. Ardizzone, R. Atlas, C.-L. Shie: Surface turbulent heat and momentum fluxes over global oceans on basis of the Goddard satellite retrievals, Version 2, *J. Climate*, 2003 in press.

Clayson, C.A., Fairall C. W., and Curry J.A., 1996: Evaluation of turbulent fluxes at the ocean surface using surface renewal theory, *J. of Geophysical Res.* Vol. 101, 28,503-28,513.

Clayson, C.A. and J. Curry, 1996: Determination of surface turbulent fluxes for the TOGA COARE: Comparison of satellite retrievals and in-situ measurements, *J. of Geophysical Res.* Vol. 101, 28515-28528.

Coppin, P.A., E. F. Bradley, I.J. Barton, and J. S. Godfrey 1991: Simultaneous observations of sea surface temperature in the western equatorial Pacific Ocean by bulk, radiative, and satellite methods, *J. Geophys. Res.*, 96, 3401-3409

Curry, J., et al.1999,: High-resolution satellite-derived data set of surface fluxes of heat, freshwater, and momentum for the TOGA COARE IOP, *Bulletin of the American Meteorological Society*, Vol. 80, 2059-2080.

Curry, J., et al., 2003: SEAFUX. *Bulletin of the American Meteorological Society* (submitted)

Darnell, Wayne L., S. Gupta, W. Staylor 1983: Downward longwave radiation at the surface from satellite measurement, *J. Climate & Appl. Meteorol.*, Vol 22, no. 11, 1956-1960.

Fairall, C.W., E.F. Bradley, D.P. Rogers, J.B. Edson, and G.S. Young, 1996: Bulk parameterization of fair-sea fluxes in TOGA COARE, *J. Geophys. Res.*, 101, 3747-3767.

Fariall, C.W., E. F. Bradley, et al. 2003: Bulk parameterization of air-sea fluxes: updates and verification for the COARE algorithm, *J. Climate*, Vol. 15, 571-591.

Flament, P., and M. Sawyer, 1995: Observations of the effects of rain temperature on the



surface heat flux in the Inter-Tropical Convergence Zone, *J. Phys. Ocean.*/ 413-419.

Gautier, C., R. Frouin, and J.-Y. Simonot, 1988: An attempt to remotely sense from space the sea surface heat budget over the Indian Ocean during the 1979 monsoon, *Geophys. Res. Lett.* 15, 1121-1124.

Goodberlet M.A. and C. T. Swift, J.C. Wilkerson, 1989: Remote sensing of ocean surface winds with the Special Sensor Microwave/Imager, *J. of Geophysical Res.* Vol. 94 14,547-14555.

Gosnell R., C.W. Fairall, P.J. Webster, 1995: The sensible heat of rainfall in the tropic ocean, *J. of Geophys. Res.*, 100, 18437-18442.

Gupta, Shashi K, 1989: A parameterization for longwave surface radiation from sun-synchronous satellite data, *J. Climat.*, Vol. 2, 305-320.

Gupta, Shashi K., Darnell, Wayne L., and Wilber, 1992: A Parameterization for longwave surface radiation from satellite data- recent improvements, *J. Appl. Meteorol.*, Vol. 31, no 12, 1361-1367.

Gupta, Shashi K., D. P. Kratz, P. Stackhouse, A. Wilber, 2001: The Langley parameterized shortwave algorithm (LSPA) for surface radiation budget studies, *NASA/TP-2001-211272*

Gupta, Shashi K., D. P. Kratz, A. C. Wilber and C. Nguyen, 2003: Validation of the Langley Parameterized algorithms for deriving CERES/TRMM surface radiative fluxes, 12th conference on satellite meteorology and oceanography, 83<sup>rd</sup> AMS annual meeting.

Inamdar, A. K., V. Ramanathan, 1994: Physics of greenhouse effect and convection in warm oceans, *J. Climat.*, Vol. 7, no. 5, 715-731.

Jones, C., P. Peterson, and C. Gautier, 1999: A new method for deriving ocean surface specific humidity and air temperature: an Artificial neural network approach, *J. Applied Meteorology*, 38, 1229-1246.

Josey, S. A. 2001: A comparison of ECMWF, NCEP-NCAR, and SOC surface heat fluxes with moored buoy measurements in the subduction region of the Northeast Atlantic, *J. of Climate*, 14, 1780-1789.

Kano, A and M. Kubota 2000: Accuracy of satellite-derived turbulent heat fluxes, *Proceedings of the 5<sup>th</sup> Pacific Ocean Remote Sensing Conference 2000*, 613-616

Kummerow C., W. Barnes, T. Kozu et al. 1998: The tropical rainfall measuring mission (TRMM) sensor package, *J. of Atmo. and oceanic Tech.*, 15, 809-817.

Kubota, M. et al. 2002: Japanese Ocean Flux data sets with use of remote sensing observation (J- OFURO), *J. of Oceanography*, Vol. 58, 213-225.

Lee, R. B., B. Barkstrom, G. Smith et al., 1996: The clouds and earth's radiation energy system (CERES) sensors and preflight calibration plans, *J. Atmos. & Ocean. Technol.*, Vol. 13, 300-313

Li, Z. H. Leighton, 1993: Global climatologies of solar radiation budgets at the surface and in the atmosphere from 5 year of ERBE data, *J. Geophys. Res.* Vol. 98, 4919-4930.

Lin, B., B. A. Wielicki, P. Minnis, and W. B. Rossow, 1998: Estimation of water cloud properties from satellite microwave, infrared, and visible measurements in oceanic environments. 1: Microwave brightness temperature simulations, *J. Geophys. Res.*, 103, 3873-3886.

Lin, B., P. Minnis, A. Fan, T. Charlock, D. Young, and Y. Hu, 2001: The surface and TOA heat budgets over tropical oceans observed by TRMM satellite, *Proc. AMS 11th Conf. on interaction of the sea and atmosphere*, May 14-18, 127-129.

Loeb, N. et al., 2001: Determination of unfiltered radiance from the Cloud and Earth's Radiant Energy System instrument. *J. Appl. Meteor.*, 40, 822-835.

Loeb, N. and coauthors, 2003: Angular distribution models for top-of-atmosphere radiative flux estimation from CERES instrument on TRMM satellite, I: Methodology, *J. of Meteor.* Vol. 42 240-264..

Liu, W. T. 1988: Moisture and latent heat flux variabilities in the tropical Pacific derived from satellite data, *J. Geophys. Res. (Oceans)*, 93, 6749-6770

Liu, W. T. and C. Gautier, 1990: Thermal forcing on the tropical Pacific from satellite data, *J. Geophys. Res.*, 95, 13209-13217, 13579-13580. Look up which pages are right ????????

Mahrt, L., D. Vickers, J. Sun, and J. McCaughey, 2001: Calculation of area-averaged Fluxes: Application to BOREAS, *J. of Appl. Meteor.* Vol. 40, 915-920

Michael, K. L., M. Nunez, 1991: Derivation of ocean-atmosphere heat fluxes in a tropical environment using satellite and surface data, *Inter. J. of Climatology*, Vol. 11, 559-575.

Minnis, P., D. P. Kratz, J. A. Coakley, Jr./ M.D. King, D. Garber, P. Heck, S. Mayor, D. F. Young, and R. Arduini, 1995: Cloud optical property retrieval. CERES algorithm theoretical basis document, NASA RP 1376 Vol. 3, pp 135-176.

Minnis, P., D.F. Young, B. A. Baum, P.W. Heck, and S. Mayor, 1997: A near-global Analysis of cloud microphysical properties using multispectral AVHRR data, *Proc. AMS*

9th Conf. Atmos. Radiation, Long Beach, CA, Feb. 2-7, 443-446.

Minnis, P., D. P. Garber, D. F. Young, R. F. Arduini, and Y. Takano, 1998: Parameterization of reflectance and effective emittance for satellite remote sensing of cloud properties, *J. Atmos. Sci.*, 55, 3313-3339.

Minnis, P., W. L. Smith, Jr., and D. F. Young, 2001: Cloud macro- and microphysical properties derived from GOES over the ARM SGP domain. Proceedings of the ARM 11<sup>th</sup> Science Team Meeting, 11 pp. (available at [http://www.arm.gov/docs/documents/Technical/conf\\_0103/minis-p.pdf](http://www.arm.gov/docs/documents/Technical/conf_0103/minis-p.pdf)).

Minnis, P., and co-authors, 2002: A global cloud database from VIRS and MODIS for CERES, Proc. SPIE 3rd Intl. Asia-Pacific Environ. Remote Sensing Symp. 2002: Remote Sens. Atmos., Ocean, Environ., and Space, Hangzhou, China, October 23-27. (<http://www-pm.larc.nasa.gov/ceres/pub/conference/Minnis.SPIE.02.pdf>).

Moore, G. W. K. and I. A. Renfrew, 2002: An assessment of the surface turbulent heat fluxes from the NCEP-NCAR reanalysis over the western boundary currents, *J. of Climate*, 15, 2020-2037.

Priestley, K, et al., 2000: Post-launch radiometric validation of the cloud and the earth's radiant energy system (CERES) proto-flight model on the tropical rainfall measuring mission (TRMM) spacecraft through 1999, *App. Meteor.*, 39., 2249-2258.

Rossow, W.B., and A.A. Lacis, Global, seasonal cloud variations from satellite radiance measurements, 2, Cloud properties and radiative effects, *J. Clim.*, 3 1204-1253, 1990

Rossow, W.B., and Y.C. Zhang, Calculation of surface and top of atmosphere radiative fluxes from physical quantities based on ISCCP data sets, 2 validation and first results, *J. of Geo. Res.*, 100, 1167-1197, 1995

Schluessel P., H.-Y. Shin, W. Emery, and H. Grassl, 1987: Comparison of satellite-derived sea surface temperatures with in situ skin measurements, *J. of Geophys. Res.* Vol. 92, 2859-2874.

Schluessel P., W. J. Emery, H. Grassl, and T. Mammen, 1990: On the bulk-skin temperature and its impact on satellite remote sensing of sea surface temperature, *J. of Geophysical Res.* 95, 13,341-13,356.

Schluessel P., H. Luthardt, 1991: Surface wind speeds over the north sea from special sensor microwave/imager observations, *J. of Geophysical Res.* Vol. 96, 4845-4853.

Schluessel P., L. Schanz and G. Englisch, 1995: Retrieval of latent heat flux and longwave irradiance at the sea surface from SSM/I and AVHRR measurements, *Adv. Space Res.* 16, No. 10, 107- 116.

- Schulz, J., P. Schluessel, and H. Grassl, 1993: Water vapor in the atmospheric boundary layer over oceans from SSM/I measurements, *Int. J. Remote sensing*, 14, 2773-2789.
- Schulz, J., J. Meyweak, S. Ewald, and P. Schluessel, 1997: Evaluation of satellite-derived Latent Heat Fluxes, *J. of Climate*, 10, 2782-2795.
- Smith, G. L., 1994: Effects of time response on the point spread function of a scanning radiometer, *Appl. Opt.*, 33, 7031-7037.
- Smith, S. R., D. M. Legler, and K. V. Verzone, 2001: Quantifying uncertainties in NECP reanalyses using high-quality research vessel observation, *J. Climate*, 14, 4062-4072.
- Stackhouse, P. W., S.K. Gupta, S.J. Cox, M. Chiacchio and J. C. Mikovitz, 2000: The WCRP/GEWEX surface radiation budget project release 2: an assessment of surface fluxes at 1 degree resolution, International Radiation symposium, St. Petersburg, Russia, 24-29 July
- Wang, W., and M.J. McPhaden, 2001: What is the mean seasonal cycle of surface heat flux in the equatorial Pacific region, *J. Geophys. Res.*, 106, 837-857.
- Webster, P. and R. Lukas, 1992: TOGA COARE: The Coupled Ocean-Atmosphere Response Experiment, *Bulletin American Meteor. Soc.* Vol. 73, No. 9, 1377-1416
- Wielicki, B. A., B. R. Barkstrom, E.F. Harrison, R. B. Lee, G. L. Smith, and J. E. Cooper, 1996: Cloud and the Earth's Radiant Energy System (CERES): an Earth observing system experiment, *Bull. Am. Meteor. Soc.*, 77, 853-868.
- Wentz, F. J., L.A. Mattrox, S. Peteherych, 1986: New algorithms for microwave measurements of ocean winds: application to SEASAT and the special sensor microwave imager, *J. of Geophys. Res.* Vol. 91, 2289-2307
- Wentz, F.J., 1997: A well calibrated ocean algorithm for SSM/I, *J. Geophys. Res.*, 102, 8703- 8718.
- Zhang, Y. C., and W.B. Rossow, Calculation of surface and top of atmosphere radiative fluxes from physical quantities based on ISCCP data sets, 1. Method and sensitivity to input data uncertainties, *J. of Geo. Res.*, 100, 1149-1165, 1995

## Appendix A

### Facts about TRMM Mission and Its Instruments

The content of this appendix is extracted from the TRMM web site:

<http://trmm.gsfc.nasa.gov/>

The Tropical Rainfall Measuring Mission (TRMM) is a joint mission between NASA and the National Space Development Agency (NASDA) of Japan designed to monitor and study tropical rainfall. The accurate measurement of the spatial and temporal variation of tropical rainfall around the globe remains one of the critical unsolved problems of meteorology. TRMM, sampling footprint between 35°N and 35°S, will provide the first detailed and comprehensive dataset on the four dimensional distribution of rainfall and latent heating over vastly under-sampled oceanic and tropical continental regimes. Combined with concurrent measurement of the atmosphere's radiation budget, estimates of the total diabatic heating will be realized for the first time ever on a global scale. The primary instruments for measuring precipitation are the Precipitation Radar (PR), the TRMM Microwave Imager (TMI), and the Visible and Infrared Scanner (VIRS). Additionally, TRMM carries the Lightning Imaging Sensor (LIS) and the Clouds and the Earth's Radiant Energy System (CERES) instrument. These instruments can all function individually or in combination with one another.

#### 1. Visible and Infrared Scanner

VIRS is one of the three instruments in the rain-measuring package and serves as a very indirect indicator of rainfall. It also ties in TRMM measurements with other measurements that are made routinely using the meteorological Polar Orbiting Environmental Satellites (POES) and those that are made using the Geostationary Operational Environmental Satellites (GOES) operated by the United States. VIRS uses a rotating mirror to scan across the track of the TRMM observatory, thus sweeping out a region 720 kilometers wide as the observatory proceeds along its orbit. Looking straight

down (nadir), VIRS can pick out individual cloud features as small as two kilometers.

VIRS, as its name implies, senses radiation coming up from the Earth in five spectral regions, ranging from visible to infrared, or 0.63 to 12 micrometers. VIRS is included in the primary instrument package for two reasons. First is its ability to delineate rainfall. The second, and even more important reason is to serve as a transfer standard to other measurements that are made routinely using POES and GOES satellites. The intensity of the radiation in the various spectral regions (or bands) can be used to determine the brightness (visible and near infrared) or temperature (infrared) of the source. The strength of the IR observations lies in the ability to monitor the clouds continuously from geostationary altitude. By comparing the visible and infrared observations on the Tropical Rainfall Measuring Mission with the rainfall estimates of the TRMM Microwave Imager and Precipitation Radar, it is hoped that much more can be learned about the relationship of the cloud tops as seen from geostationary orbit.

## 2. Clouds and the Earth's Radiant Energy System

The Clouds and the Earth's Radiant Energy System (CERES) is used to study the energy exchanged between the Sun; the Earth's atmosphere, surface and clouds; and space. The Earth's daily weather and climate are controlled by the balance between the amount of solar energy received by the Earth (both by its surface, and its atmosphere and clouds) and the amount of energy emitted by the Earth into space. Scientists have been working for decades to understand this critical energy balance - to understand the budget of incoming and outgoing energy, called the Earth's radiation budget.

A major portion of the energy received from the Sun is at short wavelengths while the majority of energy emitted by the surface of the Earth and by clouds is at long wavelengths. Increases in the amounts of greenhouse gases (gases in the atmosphere that absorb the long wavelength energy emitted by the Earth) can lead to a warming of the

Earth's surface. Such changes may, in turn, cause changes in the Earth's weather and climate. Some of the shortwave radiation from the Sun is also reflected back into space by clouds and small particles in the atmosphere called aerosols. Major sources of aerosols include windblown dust, emissions from the burning of fossil fuels such as gasoline, and the burning of forests and agricultural fields (biomass burning).

### Water Vapor Effects

The CERES instrument is based on NASA Langley's highly successful Earth Radiation Budget Experiment, which used three satellites to provide global energy budget measurements from 1984 to 1993. CERES measures the energy at the top of the atmosphere, as well as estimate energy levels within the atmosphere and at the Earth's surface. Using information from very high resolution cloud imaging instruments on the same spacecraft, CERES also determine cloud properties, including cloud-amount, altitude, thickness, and the size of the cloud particles. All of these measurements are critical for advancing our understanding of the Earth's total climate system and further improving climate prediction models. Five CERES instruments have been flown on multiple satellites starting with TRMM, followed by a launch on the Earth Observing System (EOS)-AM satellite in 1998 and the EOS-PM satellite in 2000. Follow-up CERES satellite missions are planned to create a continuous 15-year history of highly accurate energy budget and cloud data for enhanced climate analyses.

### 3. Microwave Imager

TRMM Microwave Imager (TMI) is a passive microwave sensor designed to provide quantitative rainfall information over a wide swath under the TRMM satellite. By carefully measuring the minute amounts of microwave energy emitted by the Earth and its atmosphere, TMI is able to quantify the water vapor, the cloud water, and the rainfall intensity in the atmosphere. It is a relatively small instrument that consumes little power. Combined with the wide swath and the good quantitative information regarding rainfall

make TMI the "workhorse" of the rain-measuring package on Tropical Rainfall Measuring Mission.

The TMI measures the intensity of radiation at five separate frequencies: 10.7, 19.4, 21.3, 37, 85.5 GHz. These frequencies are similar to those of the SSM/I, except that TMI has the additional 10.7 GHz channel designed to provide a more-linear response for the high rainfall rates common in tropical rainfall. TMI has a 487 miles (780-kilometer) wide swath on the surface. The higher resolution of TMI on TRMM, as well as the additional 10.7 GHz frequency, makes TMI a better instrument than its predecessors. Measuring Rainfall with Microwaves

#### 4. Precipitation Radar

The Precipitation Radar is the first space borne instrument designed to provide three-dimensional maps of storm structure. The measurements should yield invaluable information on the intensity and distribution of the rain, on the rain type, on the storm depth and on the height at which the snow melts into rain. The estimates of the heat released into the atmosphere at different heights based on these measurements can be used to improve models of the global atmospheric circulation.

The Precipitation Radar has a horizontal resolution at the ground of about 2.5 miles (four kilometers) and a swath width of 137 miles (220 kilometers). One of its most important features is its ability to provide vertical profiles of the rain and snow from the surface up to a height of about 12 miles (20 kilometers). The Precipitation Radar is able to detect fairly light rain rates down to about .027 inches (0.7 millimeters) per hour. At intense rain rates, where the attenuation effects can be strong, new methods of data processing have been developed that help correct for this effect. The Precipitation Radar is able to separate out rain echoes for vertical sample sizes of about 820 feet (250 meters) when looking straight down. It will carry out all these measurements while using only 224



watts of electric power-the power of just a few household light bulbs. The Precipitation Radar was built by the National Space Development Agency (NASDA) of Japan as part of its contribution to the joint US/Japan Tropical Rainfall Measuring Mission (TRMM)

## 5. Lightning Imaging Sensor

The Lightning Imaging Sensor is a small, highly sophisticated instrument that detects and locates lightning over the tropical region of the globe. Looking down from a vantage point aboard the Tropical Rainfall Measuring Mission (TRMM) observatory, 218 miles (350 kilometers) above the Earth, the sensor will provide information that could lead to future advanced lightning sensors capable of significantly improving weather "nowcasting."

The lightning detector is a compact combination of optical and electronic elements including a staring imager capable of locating and detecting lightning within individual storms. The imager's field of view allows the sensor to observe a point on the Earth or a cloud for 80 seconds, a sufficient time to estimate the flashing rate, which tells researchers whether a storm is growing or decaying. The sensor was developed by the Global Hydrology Center at NASA's Marshall Space Flight Center in Huntsville, Ala., in conjunction with Lockheed Martin, Palo Alto, Calif., and Kaiser Electro Optics, Carlsbad, Calif. The Lightning Imaging Sensor is approximately eight inches in diameter and 14 inches high, while the supporting electronics package is about the size of a standard typewriter. Together, the two modules weigh approximately 46 pounds and use about 25 watts of power.

## VITA

Tai-Fang (Alice) Fan

Born in Tainan, Taiwan, October 17, 1950. Graduated from National Taiwan University, 1974. Came to United States 1982. M.S. Computer and Information Science, University of Florida, Gainesville, Florida, 1985. Have worked for NASA Langley contractors since 1987. In 1996, the author entered the College of William and Mary as a part time graduate student.